Ore Geology Reviews 112 (2019) 103027

Contents lists available at ScienceDirect

Ore Geology Reviews

journal homepage: www.elsevier.com/locate/oregeorev

REE concentration processes in ion adsorption deposits: Evidence from the Ambohimirahavavy alkaline complex in Madagascar

Guillaume Estrade[a,*], Eva Marquis[b], Martin Smith[b], Kathryn Goodenough[c], Peter Nason[b]

[a] GET, University of Toulouse, CNRS, IRD, UPS, (Toulouse), France
[b] School of Environment and Technology, University of Brighton, Brighton, UK
[c] British Geological Survey, The Lyell Centre, Edinburgh EH14 4AP, UK

ARTICLE INFO

Keywords:
Ion-adsorption deposit
Laterite
Rare-earth elements
Clays
Alkaline complex
Madagascar

ABSTRACT

Ion adsorption deposits, in which the rare earth elements (REE) occur adsorbed onto clay mineral surfaces, currently provide the world's dominant supply of heavy REE (Gd-Lu). Concentration of REE within ion adsorption deposits has been proposed to be a dominantly supergene process, where easily degradable REE-minerals (e.g. REE-fluorcarbonates) break down and release REE that are then adsorbed onto clay mineral surfaces in the weathered material. Here we present data from the Cenozoic Ambohimirahavavy alkaline complex in Madagascar, with the aim of further constraining controls on the formation and HREE enrichment processes in ion adsorption deposits.

The laterite weathering profiles described here are developed on alkaline igneous rocks, including both SiO_2-undersaturated and oversaturated lithologies. The latter group includes REE mineralised peralkaline granitic pegmatites and granitic dykelets. The weathering mineralogy includes gibbsite, clay minerals and minor Fe and Mn oxyhydroxides. X-ray diffraction and infrared spectroscopy show that the clay fraction in all sites is dominated by kaolinite and halloysite (7 Å and 10 Å). Extraction with ammonium sulfate (0.5 M $(NH_4)_2SO_4$, pH = 4; removes weakly adsorbed metals retained on the solid surface and dissolves carbonates) indicates that, in the different profiles and along the same profile, the leachable REE content is heterogeneous, ranging from 5 to 2300 mg/kg total REE, with 1 to 32% heavy REE. Leaching with magnesium chloride (0.5 M $MgCl_2$, pH = 6; removes only weakly adsorbed REE) releases similar total REE concentrations, suggesting that most of the leachable REE are adsorbed onto mineral surfaces. In most of the laterite profiles, the amount of leachable REE continuously increases with depth up to the saprock. Recovery rates depend on the REE atomic number, generally decreasing from La to Lu except for Ce which is invariably low.

In the Ambohimirahavavy complex, the nature of the protolith is the main factor controlling the amount of easily leachable REE in the laterite weathering profile. Hydrology and topography are secondary factors. The most favourable protoliths include SiO_2-undersaturated volcanic lithologies and altered mudstone with granitic dykelets. The main primary REE minerals include agpaitic minerals (eudialyte) and allanite-(Ce). Locally in granitic pegmatite dykes, autometasomatism by late magmatic fluids inhibits formation of ion adsorption ore by transforming easily weathered agpaitic minerals into unweatherable zircon.

1. Introduction

The rare earth elements (REE) have been the subject of substantial research in recent years, due to their importance as 'critical metals' used in a range of modern technologies (Chakhmouradian and Wall, 2012; Goodenough et al., 2017). REE deposit types include both hard-rock deposits most commonly associated with carbonatites and alkaline rocks, and deposits formed by lower-temperature processes of erosion and weathering (Goodenough et al., 2017). The lower-temperature deposits, which include placers, bauxites and ion-adsorption deposits, are lower grade but have the potential to be more easily mined and processed than hard-rock deposits (Wall et al., 2017). Here we investigate the controls on ion adsorption deposit formation, using a case study in North Madagascar.

Ion adsorption-type REE deposits (IADs) are typically formed by the sub-tropical weathering of igneous rocks that contain primary and/or secondary REE-minerals. In these weathered deposits, the REE are mainly adsorbed onto the surface of clays (kaolinite and halloysite) but

* Corresponding author.
E-mail address: guillaume.estrade@get.omp.eu (G. Estrade).

https://doi.org/10.1016/j.oregeorev.2019.103027
Received 15 March 2019; Received in revised form 9 July 2019; Accepted 19 July 2019
Available online 20 July 2019

may also be contained in the structures of secondary minerals (Sanematsu and Kon, 2013). The processes of REE adsorption to the clays are complex and affected by a number of factors (Li et al., 2017). These deposits are low grade, ranging from 300 to 3500 ppm total rare earth oxides, and generally smaller than other REE deposits (0.5–0.01 Mt). A few IADs have a high proportion of the most valuable heavy REE (HREE) (Bao and Zhao, 2008; Li et al., 2017) and these currently supply most of the world's demand for HREE. The REE in IADs are easily released by low cost ion-exchange processes, either by *in-situ* leaching or heap leaching with acid electrolyte solutions (Moldoveanu and Papangelakis, 2016). Most of these deposits are currently mined in Southern China (source of almost all the world's HREE), but recently discovered potential IADs are under exploration in South America, Africa, and Southeast Asia (Sanematsu and Watanabe, 2016).

Factors influencing the formation of IADs are climate, topography, bedrock composition and the length of time exposed in a stable environment. Previous studies have shown that REE are leached from the top of the profile and accumulated in intermediate horizons (Bao and Zhao, 2008; Janots et al., 2015; Sanematsu and Watanabe, 2016). These studies rely on limited sampling and few deposits outside China have been studied in detail.

In presently mined IADs, the extraction of REE is mainly achieved by in-situ or heap leaching with moderately acid (pH ~ 4) ammonium sulfate solution (Moldoveanu and Papangelakis, 2016). These extractive processes are favoured because of their low costs and their ease of implementation but have a major impact on the environment (Packey and Kingsnorth, 2016; Yang et al., 2013).

In this paper, we assess a potential IAD from north-west Madagascar. The mineralized lateritic regolith is derived from the weathering of alkaline igneous rocks from the Cenozoic Ambohimirahavavy alkaline complex. Representative hand excavated pits and core profiles have been sampled across the complex for a detailed mineralogical study, associated with an ammonium sulfate extraction, with the aim of better identifying the REE-bearing phases and understanding the genesis of the IAD. Early research into Chinese IAD has suggested that the protoliths were relatively simple granitoids (Bao and Zhao, 2008). More recently it has been demonstrated that the most HREE enriched deposits underwent pre-weathering enrichment via magma mixing, metasomatic alteration or both, involving non-granitic sources of the REE (Xu et al., 2017). An additional goal in our study was to test the hypothesis that IAD characteristics may be protolith specific, and that igneous protoliths with an association with REE mineralisation (syenites) may result in higher grades of adsorbed REE in lateritic regolith.

2. Geological setting

The geology of Madagascar is dominated by Precambrian basement, with the western-most part of the country covered by Mesozoic sedimentary rocks of the Majunga, Mailaka and Morondava sedimentary basins (Geiger and Schweigert, 2006). The Ambohimirahavavy alkaline complex belongs to the Cenozoic North Alkaline Province of Madagascar, which comprises several intrusive and extrusive igneous massifs hosted by both Mesozoic sedimentary rocks and Precambrian basement (Fig. 1). These can be divided broadly into the intrusive rocks of the Ampasindava Suite, and the volcanic rocks of the Ankaizina Group (BGS-USGS-GLW, 2008).

The alkaline igneous intrusions of the Ampasindava Suite are emplaced in and around the Ampasindava peninsula, and are largely hosted by Mesozoic sedimentary rocks. This suite essentially comprises intrusions of gabbro, nepheline syenite, syenite, quartz syenite and alkali granite, which are Miocene to Oligocene in age (Cucciniello et al., 2016). To the north-east and south-east of the Ampasindava peninsula, the massifs are mainly composed of Ankaizina Group volcanics which range from basaltic to phonolitic and rhyolitic compositions (BGS-USGS-GLW, 2008; Melluso et al., 2007). This region is subjected to a tropical humid climate with annual mean temperatures ranging from 20 to 27 °C and annual rainfall of *c.* 1500 mm/a (Davies, 2009). Such a climate is favourable to the development of a dense vegetation cover and a deep regolith.

The Ambohimirahavavy complex is one of four major alkaline complexes (together with Manongarivo, Bezavona and Andranomatavy) cropping out in the Ampasindava peninsula. It consists of both silica under- and oversaturated lithologies of extrusive and intrusive igneous origin (Fig. 1) (Estrade et al., 2014a). The complex is made up of two main composite felsic intrusions: (1) a north-western syenitic intrusion with subordinate quartz syenite and granite and (2) a south-eastern, circular, mostly syenitic intrusion with minor amounts of nepheline syenite, quartz syenite and granite. The south-eastern intrusion forms a ring intrusion delimiting a central circular depression. The central and northern part of the complex and the circular depression in the south-east are mainly covered with pyroclastic rocks, with subordinate trachytic to phonolitic lava flows and rare trachytic to rhyolitic lava domes (Estrade et al., 2014a). A dense network of dykes intruded into Mesozoic sedimentary rocks around the south-eastern circular intrusion includes trachytic, granitic and granitic pegmatite dykes (Estrade et al., 2014b). The south-east part of the complex is by far the most well-known area because of recent exploration works including boreholes and trenches.

The most evolved intrusive rocks in the south-eastern part of the complex, i.e. granite, nepheline syenite and granitic pegmatite dykes, are the main REE-bearing lithologies. Among them, REE mineralization associated with granitic pegmatite dykes has been recently investigated in detail (Estrade et al., 2018, 2014b; Ganzeev and Grechishchev, 2003) and their economic potential as REE ores has been assessed by Tantalus Rare Earths AG. The main REE-bearing minerals in these rocks comprise a secondary paragenesis of REE-fluorcarbonates, zirconosilicates, silicates and oxides with minor phosphates. These minerals occur mainly as pseudomorphs after eudialyte, a complex REE-Na-zirconosilicate (Estrade et al., 2018).

The whole of the Ambohimirahavavy complex has been affected by significant tropical weathering, with the generation of a lateritic regolith layer up to 12 m thick. This paper focuses on understanding the potential of this lateritic regolith for REE resources.

3. Sampling strategy

The selection of laterite sampling sites for this work has been guided by the geology and the topography of the complex, and the results from the exploration works achieved by Tantalus Rare Earths AG. Since 2012, the company has completed 4412 pits (up to 10 m deep) and 359 boreholes (up to 130 m deep) providing a set of geological and geochemical data extending across the entire complex. These data have been used to build a 3D geological model and calculate a mineral resource of 197 Mt at 897 ppm total rare earth oxide (measured + indicated; Desharnais et al., 2014). Based on this model and whole-rock REE analyses, we selected samples from four boreholes (TAND-044, TAND-097, TAND-109 and TAND-007 hereafter referred as BH1, BH2, BH3 and BH4, Fig. 1) and from four newly excavated pits (P1, P2, P3 and P4, Fig. 1), all located in the south-eastern part of the complex. The four boreholes are situated on the seaward slope of the syenitic ring intrusion, which forms a conspicuous ridge. All four boreholes transect the laterite section and enter the bedrock, which includes syenite, trachyte, mudstone, granitic pegmatite dykes and dykelets. The four pits are located along a south-west to north-east transect extending from the centre of the circular depression to the outer flank of the complex. Their precise location was chosen to assess the effect of both bedrock composition and topography on the formation of IAD. We completed our sampling with material from two well-exposed road sections (RS1 and RS2, Fig. 1). Samples from these localities have been used to build up a clear understanding of the regolith profile over the most mineralised area of the complex.

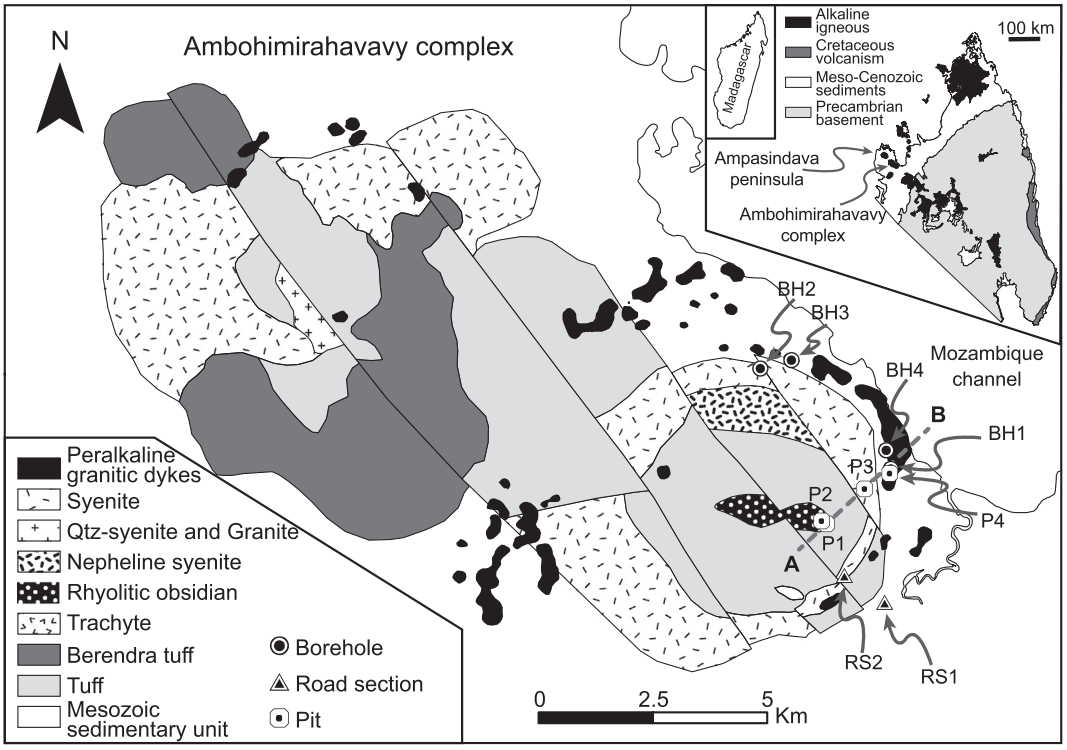

Fig. 1. Geological map of the Ambohimirahavavy complex with the location of the 4 boreholes, 4 pits and 2 road sections sampled. Inset shows the position of the complex in North Madagascar. Modified after Estrade et al. (2014a).

4. Regolith description

The regolith overlying the Ambohimirahavavy complex can be typically described as a laterite profile, i.e. a weathering profile showing some or all of the following, from the bottom up: bedrock, saprock, saprolite, mottled zone, ferruginous zone and soil (Eggleton, 2001). In this study, we adopted the following description for these terms (Eggleton, 2001):

- **bedrock** is a solid rock which has not been affected by weathering;
- **saprock** is a compact, slightly weathered rock with low porosity and < 20% of the weatherable minerals altered. It is distinguished from saprolite on the basis of its rock-like physical strength;
- **saprolite** is weathered bedrock in which the original fabric is retained with typically > 20% of weatherable minerals altered;
- the **mottled zone** typically has a mottled appearance of white, clay-rich, and red, iron stained patches;
- the **ferruginous zone**, usually red, is principally composed of secondary oxides and oxyhydroxides of iron and hydroxides of aluminium with variable amounts of clays, other secondary minerals and resistant primary minerals. The actual total Fe content is relatively low, but the presence of iron oxyhydroxides gives the zone a distinctive red-brown colour.
- **Soil**, usually brown, is the unconsolidated matter at or near the surface that has been subjected to and influenced by genetic and environmental factors such as climate, macro- and microorganisms and topography and typically has a high organic content derived from plant matter including roots.
- The mottled zone, ferruginous zone and soil are grouped into the '**pedolith**', which is the upper part of the regolith that has been subjected to soil-forming processes resulting in the loss of the fabric of the parent rock. The limit between saprolite and pedolith corresponds to the disappearance of lithic fabric.

The laterite profiles discussed here formed under a seasonal humid tropical climate that is typical for north-western Madagascar. We consider that these laterite profiles are largely autochthonous i.e. result from in-situ weathering of the underlying bedrock. There is relatively little evidence for soil transport downslope.

4.1. Boreholes

In boreholes, the laterite profile depth (the base of the saprock) ranges from 8 to 12 m (Fig. 2). The depth to the mottled zone is generally around 3 m, although in BH1 it is considerably deeper at 7 m. The composition and colour of the profile varies with depth, depending on the nature of the bedrock. In BH1, the bedrock is mainly composed of syenite and trachyte dykes intruding mudstone. In BH2, the bedrock is largely dominated by syenite whereas in BH3 and BH4 it mainly comprises mudstone with granitic dykelets. Except in BH2, these lithologies are intruded by late granitic pegmatite dykes and granitic dykelets ranging in average thickness from a few centimetres to meters.

4.2. Pits

The positions of the pits are shown on the geological map in Fig. 1 and reported on a schematic cross-section in Fig. 3. P1 and P2 are located in the central depression on a shoulder of a hill (Figs. 1 and 3). The precise nature of the bedrock directly beneath the pits is unknown, but based on the nature of surrounding outcrops and boulders, bedrock is assumed to be mainly volcanic (tuff, rhyolite and microsyenite). P3 was dug on a flat area on the top of the syenitic ring intrusion. P4 is situated on the seaward slope of the syenitic ridge facing the Mozambique Channel next to BH1. The bedrock in this pit is similar to BH1. The maximum depth reached in hand-excavated pits (ranging from 3 to 6 m) was limited by both the hardness of the material and by safety considerations. The base of the pits is typically in the well-consolidated saprolite, but they do not reach consistent saprock. As in the boreholes, the depth to the mottled zone is generally around 3–4 m.

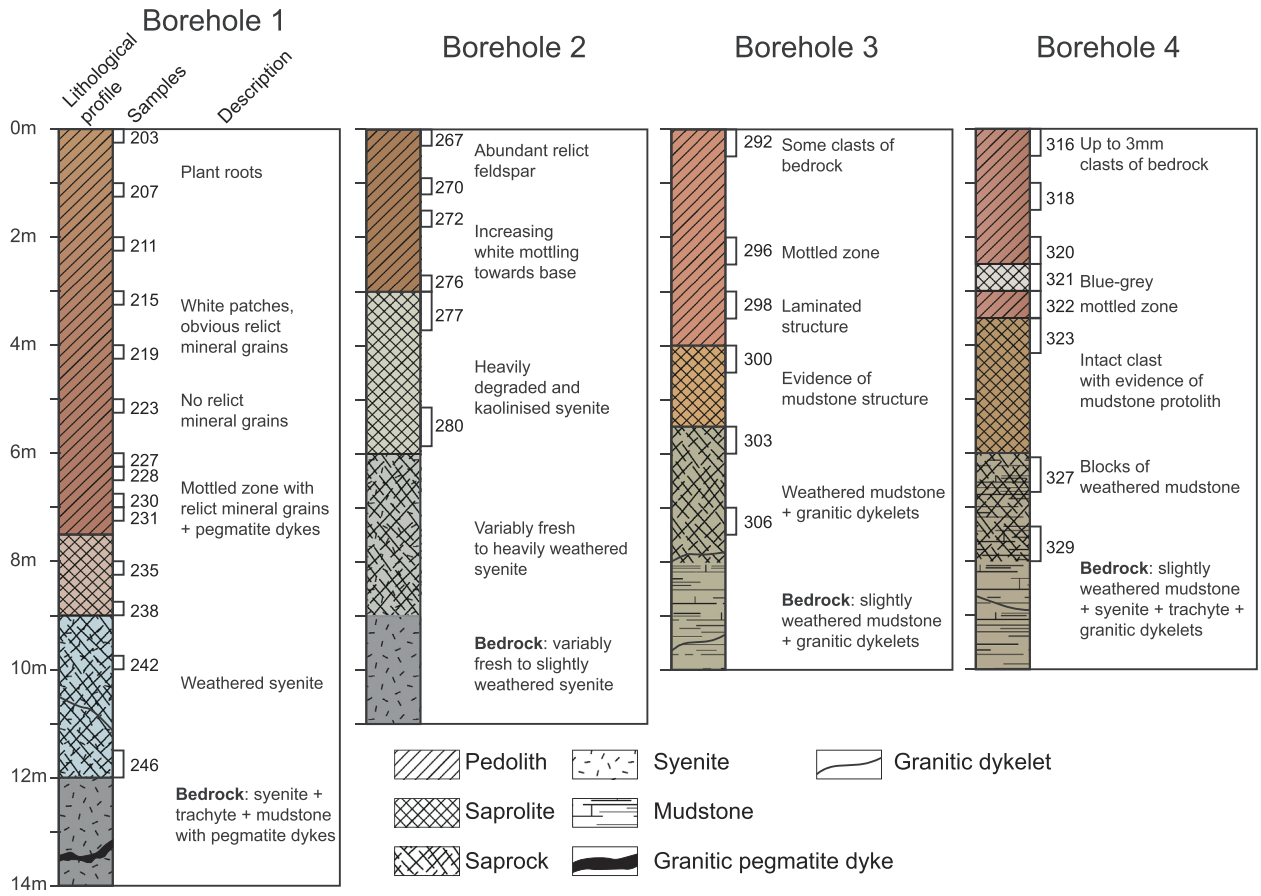

Fig. 2. Detailed log from the 4 boreholes with the position of the samples. Colours in the log are representative of the colour of the sample material.

4.3. Road sections

Road section 1 provides a freshly well-exposed laterite profile on the edge of the complex (Fig. 4). It shows a relatively thick saprolite section (> 4m thick) overlain by a thin pedolith (< 1m). The saprolite consists of two major whitish felsic dykes (> 5m thick) cutting through light-brown sedimentary rocks (here, mainly mudstone). The contact between the two lithologies is clearly visible with an apparent dip ranging from 40° to 60° towards the north-east. Two late light greenish mafic dykes (c. 1 m thick) intrude into the felsic dykes.

Road section 2 exhibits a freshly exposed laterite profile formed on the syenitic ring intrusion. It shows a 2 m-thick pedolith, varying in colour from red to yellow, overlying the top of the saprolite, which is composed of altered trachytic to syenitic rock.

5. Material and methods

5.1. X-ray diffraction and oriented preparation

X-ray powder diffraction (XRD) data were collected at the University of Brighton (UK) using a Panalytical MRD X'pert Pro High Resolution powder diffractometer in Bragg-Brentano geometry using Ni-filtered Cu-Kα radiation. Tube conditions were 40 kV and 40 mA. Randomly oriented powders were prepared using approximately 10 g of dried bulk sample which was manually ground in an agate bowl to produce a homogenous fine powder. The fine powder was then pressed into a steel ring to get a mechanically stable sample. The mounts were typically X-rayed from 5° to 70° 2θ at a scanning rate of 0.01 degrees per minute. Detection limit is approximatively 2% of sample.

The clay fraction of selected samples was separated and further characterized. The clay fraction was isolated by repeatedly mixing a few grams of sample with a solution of deionized water saturated with a dispersive agent (Na hexametaphosphate). The suspension was treated for 120 s with an ultrasonic bath to increase clay dispersion and centrifuged at 750 rpm for 260 s. The supernatant containing the clay fraction was collected and centrifuged at 3500 rpm for 30 min. The supernatant was then discarded and a few drops of deionized water were added to the clay concentrate. Slides of well-oriented clay were made by putting a few drops of the clay suspension on glass slides which were then air-dried.

5.2. Fourier transform infrared spectroscopy

Separated clays were further characterised by Fourier transform infrared spectroscopy (FT-IR) using a Nicolet Avatar 320 FT-IR at the University of Brighton (UK). Spectra were recorded over the range 4000 to 650 cm^{-1} to ensure that most of the diagnostic vibrations active in the infrared would be included.

5.3. Scanning electron microscope

Selected thin sections and polished blocks from the regolith samples were imaged using a Zeiss EVO LS15 scanning electron microscope (SEM) at the University of Brighton (UK) and a LEO 535VP SEM at the British Geological Survey (UK). Operating conditions were 20 kV with a working distance of 15 mm with variable vacuum conditions. Elemental maps were obtained using an INCA 450 energy dispersive micro-analyzer.

5.4. Ammonium sulfate and magnesium chloride extraction

To determine the exchangeable fraction of metals in the different

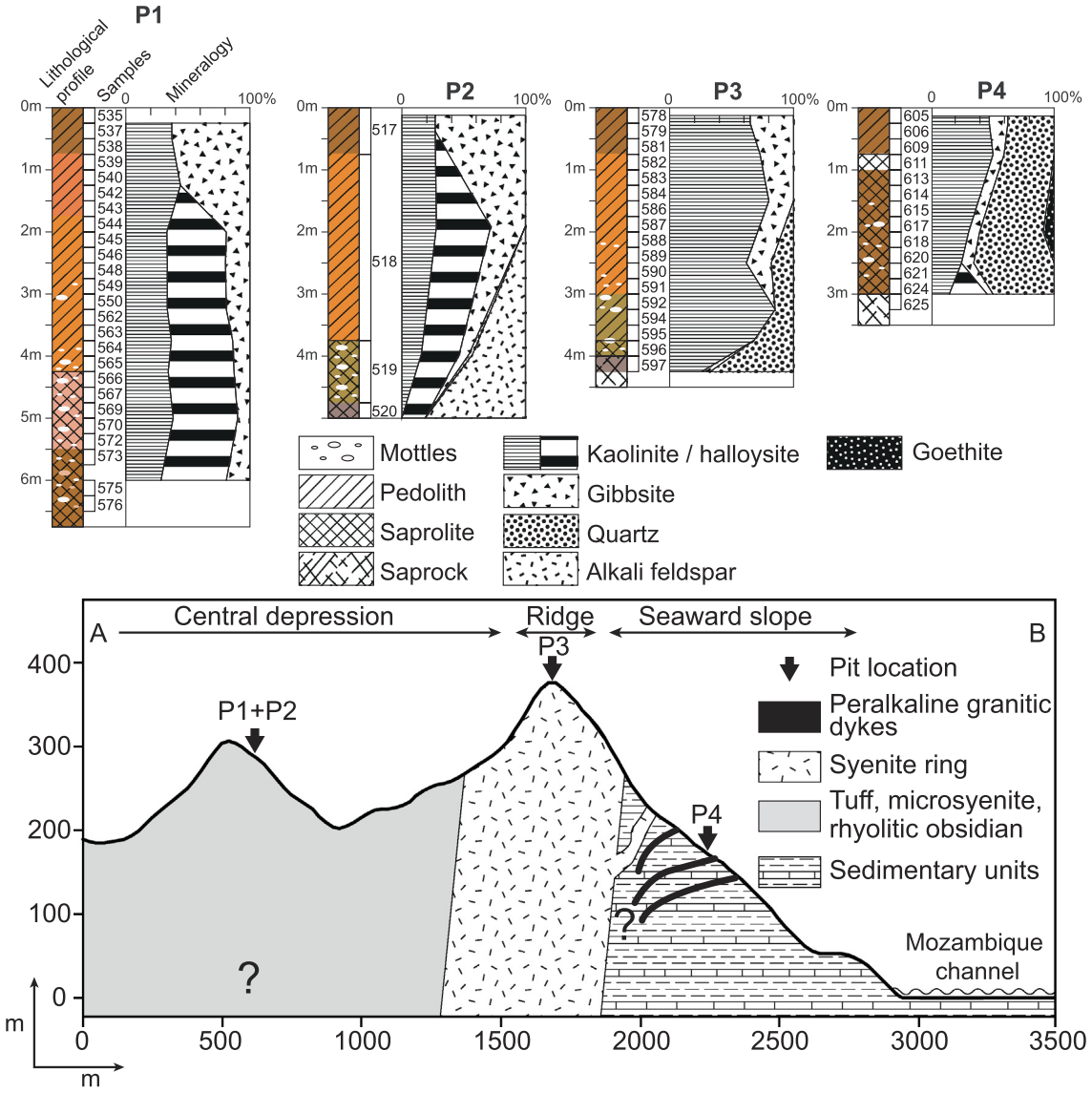

Fig. 3. Detailed logs from the 4 pits with the position of the samples and the schematic geological cross-section with the location of the pits. Note that vertical and horizontal scale in the cross-section are different. Colours in the logs are representative of the colour of the sample material. The main minerals in the sample (analysed by XRD; see methodology) are also shown in the logs.

regoliths, selected powdered samples were reacted with 2 different solutions: (1) an ammonium sulfate solution (0.5 M $(NH_4)_2SO_4$ adjusted at pH 4 with H_2SO_4) to remove the weakly absorbed metals retained on the solid surface by ion-exchangeable processes. This solution is the main reagent used by the industry to recover REE from currently mined IAD's but because of its acidic pH it can also dissolve carbonates and release associated REE. To target only the ion-exchangeable fraction and distinguish this from that hosted in secondary REE minerals, we used (2) a magnesium chloride solution with a near neutral pH (1 M $MgCl_2$ at pH 6).

One gram of each sample was dried in an oven (105 ± 2 °C) until constant weight and mixed with 40 mL of solution in a 50 mL centrifuge tube. The mixture was immediately shaken at 30 ± 10 rpm for one hour using a mechanical end-over-end shaker at room temperature. The extract was separated from the solid residue by centrifuging at 3000 g for 20 min. The solution obtained was filtered through 0.22 µm syringe filters and the filter was washed with 50 mL deionized water. Samples were stored in a fridge at 4 °C prior to analysis. For each batch of 14 samples, a blank was prepared following the same procedure. No certified reference material exists for REE leaching experiments, but repeat analyses of BCR701 (Rauret et al., 2001) showed that leaches reproduced values within 5% precision.

5.5. Inductively coupled plasma mass spectrometry

Concentrations of elements of interest in the exchangeable fraction were determined using a quadrupole based inductively coupled plasma mass spectrometer (ICP-MS, Agilent 7900) at the University of Brighton. The octopole reaction system was operated in He mode to reduce polyatomic interferences. A multi-element calibration standard (8500–6944 Agilent) was diluted with 2% nitric acid to calibrate the REE from 1 µg/L to 500 µg/L. Internal standard (Rh) was added via the online internal standard solution to all standards, samples and blanks. Subsequently the eluent solutions were analysed for major elements and other common trace elements using the same procedure and a multi-elements standard solution (8500-6940 Agilent).

5.6. Whole-rock analyses

The samples were dried at 40 °C, disaggregated and milled for loss

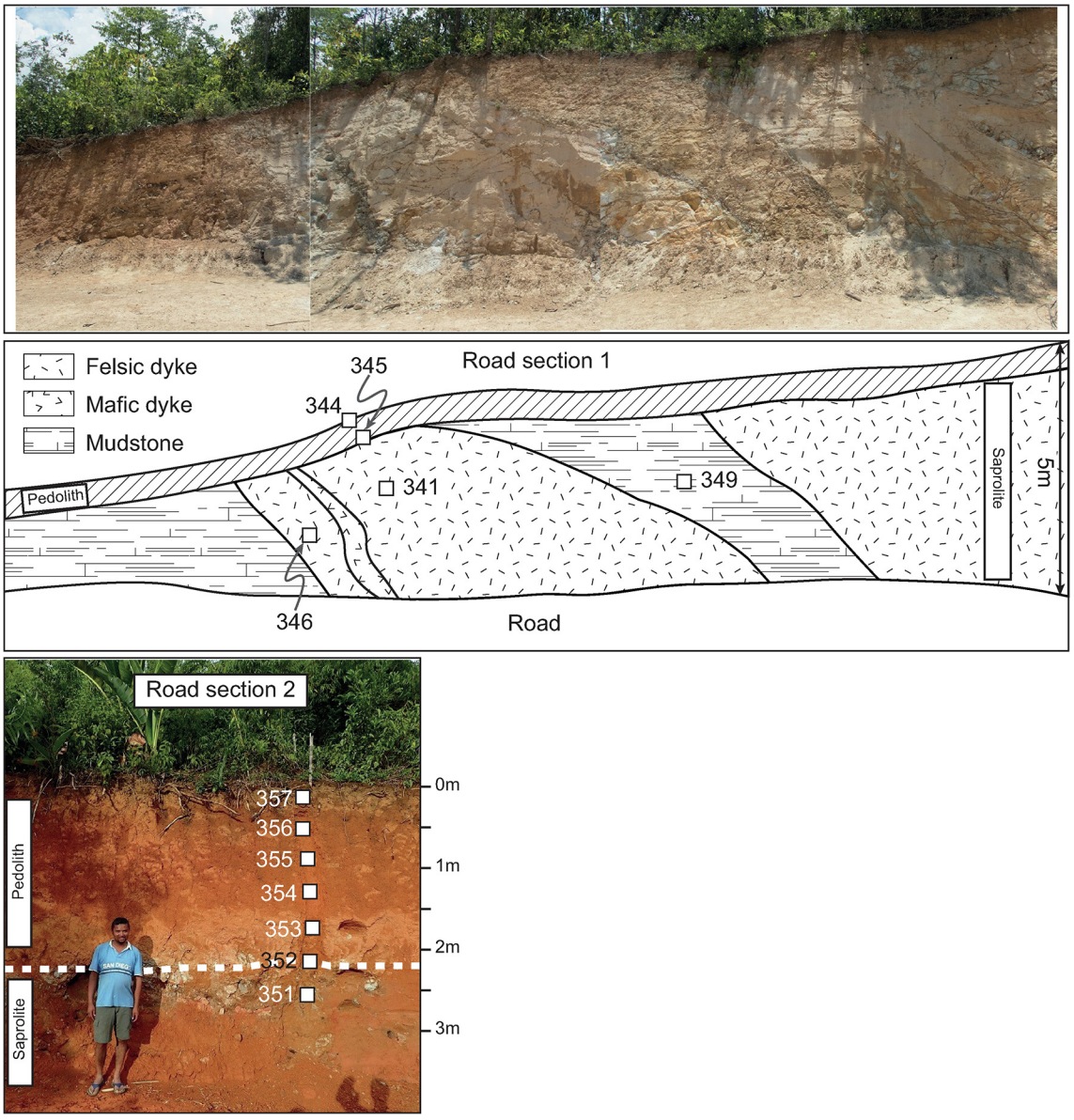

Fig. 4. Photograph and interpretation of road section 1 and road section 2 with the location of the samples.

on ignition and digestion. Samples were analysed by sodium peroxide fusion with an ICP-MS finish using a quadrupole based inductively coupled plasma mass spectrometer (ICP-MS, Agilent 7900) at the British Geological Survey. The sodium peroxide fused material was dissolved in dilute hydrochloric, nitric and hydrofluoric acids and solutions were stored in plastic Nalgene® bottles prior to analysis.

6. Results

6.1. Mineralogical composition

6.1.1. X-ray diffraction-bulk samples

The mineralogy of the igneous bedrock is dominated by alkali feldspar and quartz or nepheline, with sodic amphibole and pyroxene plus a range of accessory minerals (Estrade et al., 2014a). During tropical weathering these minerals break down at different rates (Brantley, 2008), with clay minerals being the main eventual product. Representative powder X-ray diffraction (XRD) patterns are shown in Fig. 5 (The whole XRD patterns are available as supplementary material). The main mineralogical phases detected in the pedolith of most profiles include the kaolin-group clays kaolinite and halloysite (including 10 Å-halloysite and 7 Å-halloysite), gibbsite, and quartz. Quartz was not detected in samples from the central depression (P1 and P2) except for a small amount in one sample in P2 which we attribute to quartz veins or secondary silica. Minor phases (< 5%) include Fe oxide (hematite) and hydroxide (goethite). Zircon is locally present. Feldspars (K- and Na-feldspars) are rarely detected in the pedolith but present in the saprolite. Storage of borehole cores in dry conditions precludes any accurate quantification of kaolin-group clays in these samples, as 10 Å-halloysite could have been partially dehydrated to 7 Å-halloysite. On the other hand, samples from the newly excavated pits did not suffer any dehydration and were suitable for quantitative mineralogy. Based on reference intensity ratios, semi-quantitative powder XRD analyses in P1 and P2 indicate a decreasing content of gibbsite from the top of the pedolith (> 60%) down to the saprolite (< 20%), and a correspondingly increasing content of kaolin-group clays downward. Halloysite detection starts around 1 m deep and remains relatively constant downward. In P3, the upper 1.5 m are dominated by kaolinite (> 60%) and gibbsite, then an increasing quartz proportion is detected from 1.5 m down to the saprolite (> 60%). In P4, the quartz content ranges from 35 to 65%. Kaolinite content ranges from 50% to 15% and

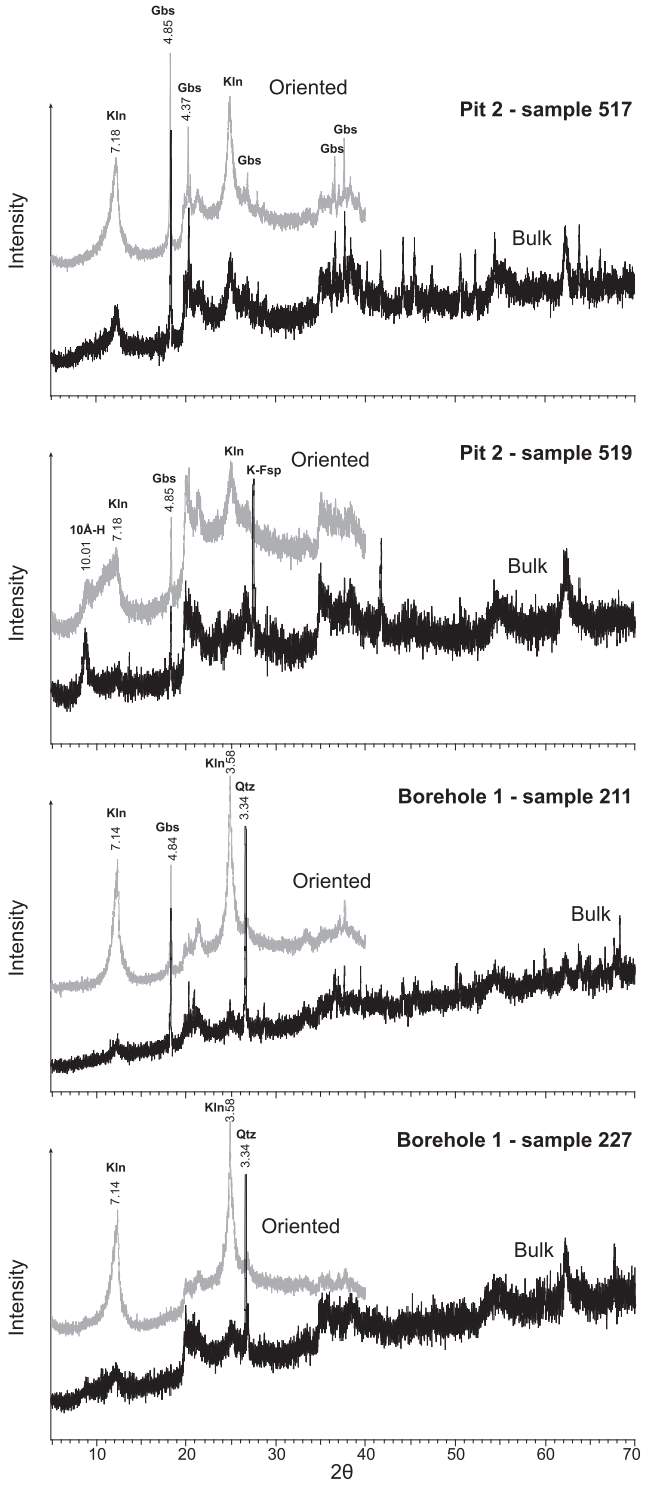

Fig. 5. X-ray diffraction patterns from representative regolith samples in pit 2 and borehole 1.

halloysite is detected in the metre above the pedolith-saprolite contact.

6.1.2. X-ray diffraction-oriented samples

We performed a detailed study on separated clays in order to identify the different type of clays present in the laterite profile of the boreholes. Representative oriented clay XRD patterns are shown in Fig. 5 (all oriented XRD patterns are shown as supplementary material in Appendix A). The main clays present in the boreholes are the kaolin-group clays kaolinite and halloysite. Kaolinite is easily identifiable with its two prominent peaks at 7.15–7.20 Å and 3.58–3.57 Å corresponding to 001 and 002 basal reflections respectively. The 001 basal reflection is usually characterised by a broad shape which could reflect high structural disorder or small size of the kaolinite analysed. Halloysite is mainly detected in saprolite as 10 Å-halloysite with its 001 basal reflection at approximatively 10.1–10.0 Å. In pedolith, the offset of the kaolinite 001 basal reflection toward higher d-values (from 7.15 to 7.20 Å to 7.3 Å) and the relatively broad peak widths could also indicate the presence of 7 Å-halloysite which may have been formed by dehydration of 10 Å-halloysite (Hillier et al., 2016).

6.1.3. FT-IR

The FT-IR spectra from separated clay samples all show the characteristic OH-stretching absorption bands for the kaolin-group minerals in the 3700–3600 cm^{-1} region (Fig. 6). The two strong bands at ~3694 cm^{-1} and ~3620 cm^{-1} are related to the in-phase stretching mode of inner-surface OH groups and of inner OH groups in kaolinite, respectively (Madejová, 2003; Russell and Fraser, 1994). The two weak absorption bands visible in most of the spectra at *ca* ~3667 cm^{-1} and ~3652 cm^{-1} are also compatible with kaolinite and related to the two out-of-phase stretching modes of inner-surface OH groups. The absence of these two bands in some samples (e.g. 279 and 321) indicate that 10 Å-halloysite is present rather than kaolinite. However, because FT-IR spectra of disordered kaolinite and halloysite exhibit very similar absorption bands, it is not possible to assess the relative content of these two clay minerals. The group of four bands in the 3600–3300 cm^{-1} region common to most of the pedolith samples except for BH3, is attributed to OH-stretching in gibbsite.

6.1.4. SEM – residual and secondary REE minerals

The nature of REE-bearing minerals varies both with depth from the pedolith to the bedrock and with the nature of the bedrock. The regolith formed by weathering of lithologies with granitic pegmatite dykes (e.g. BH1) is characterized by the abundance of residual zircon (Fig. 7A–C). In the pedolith, this weathering-resistant mineral is the most common residual REE-bearing phase and is usually associated with quartz. It is characterized by unusual textures (e.g. porous and dendritic grains, Fig. 7B-C) providing indications about the nature of the protolith. Indeed, zircons with similar textures have been described in granitic pegmatite dykes in previous studies (Estrade et al., 2014b). Approaching the pedolith-saprolite transition, less resistant REE-bearing minerals such as fergusonite-(Y) and pyrochlore-group minerals have been preserved from weathering (Fig. 7D). The least resistant minerals such as REE-fluorcarbonates are only observed in the saprolite and deeper (Fig. 7E to H). REE-bearing minerals in a granitic dykelet from BH3 bedrock consist mainly of allanite-(Ce), REE-fluorcarbonates, britholite, pyrochlore-group minerals and zircon (Fig. 7I). No residual REE-bearing minerals have been observed in laterite profiles formed mainly from trachyte weathering (RS2). In the boulders next to P1 and P2, considered as representative of the bedrock, the main REE bearing mineral identified is a REE-Ca-phosphate (Fig. 7J-K) probably representing the weathering product of monazite (Fig. 7L). In P2 saprolite, secondary Mn-Fe oxides with Ce-rich patches have been observed (Fig. 8). High Ce content is correlated with low Mn content suggesting that Ce is substituting for Mn, or occurring as cerianite (CeO_2).

6.2. Whole-rock composition

Sixty two samples were selected in the different boreholes, pits and road sections for whole-rock major and trace element analyses. All the chondrite-normalized bulk REE patterns have a negative Eu anomaly and are enriched in the LREE relative to the HREE with a slightly negative LREE slope ($1 < La_N/Sm_N < 10$) and a relatively flat HREE portion ($0 < Gd_N/Yb_N < 3$) (Fig. 9). Most of the laterite profiles show a positive Ce anomaly in their upper part which tends either to decrease in intensity or reverse to a negative anomaly with depth. At the top

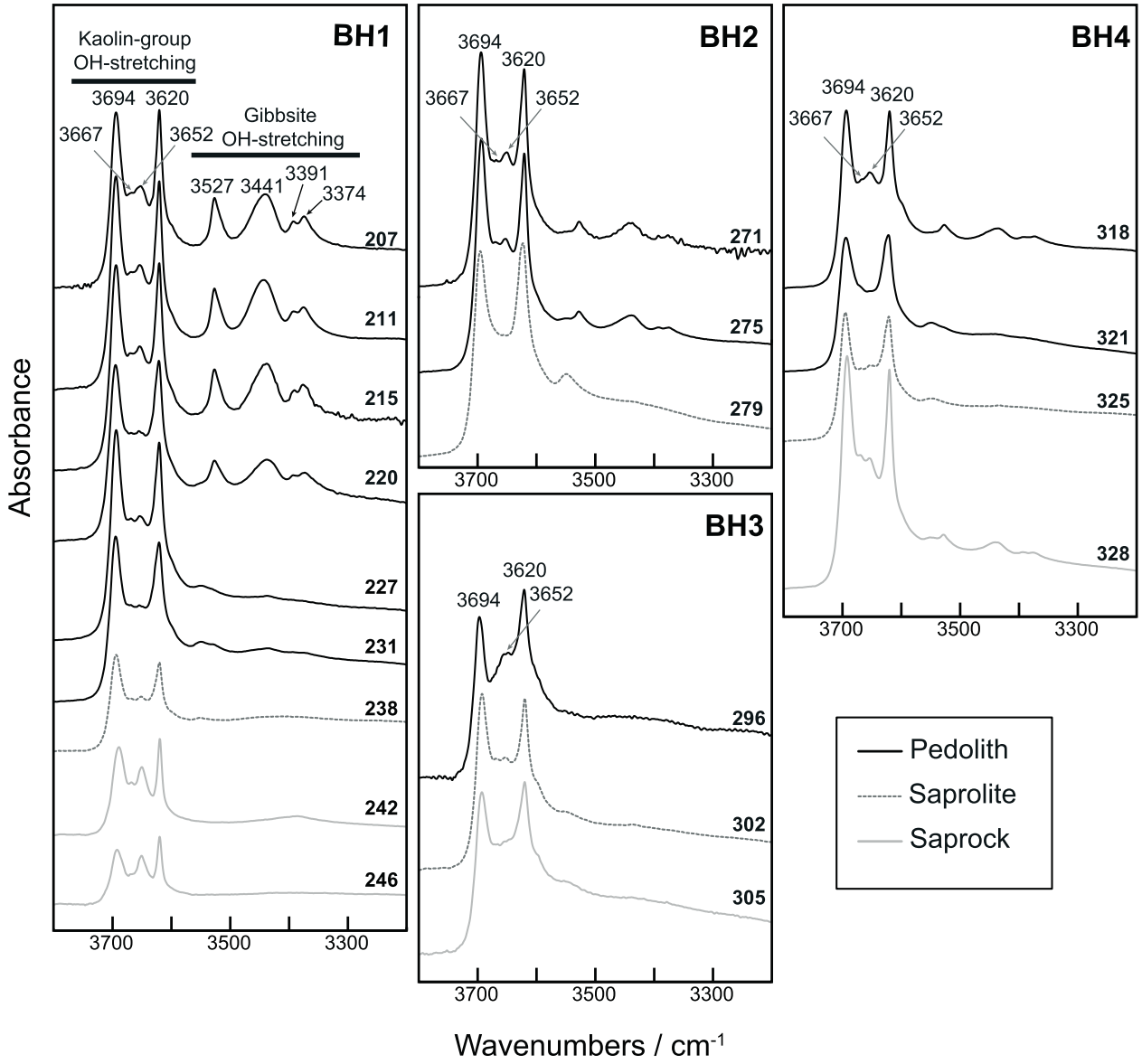

Fig. 6. Fourier Transform Infrared spectra in the region 3800–3200 cm^{-1} from representative regolith samples in the 4 boreholes.

ridge site (P3), this positive Ce anomaly is constant from the pedolith to the saprock.

Although the precise nature of the protolith is unknown for most of the regolith samples, we classified them according to their inferred protolith based on the nature of the protolith identified in the saprolite and the saprock, the geological knowledge of the complex resulting from previous mapping campaigns and by comparing whole-rock composition of regolith samples with whole-rock data of fresh samples of the main igneous lithologies of the Ambohimirahavavy complex (Fig. 10) (Estrade et al., 2014a). Zirconium can be considered as an immobile element during weathering processes (Hodson, 2002), and thus can be used as a proxy for the nature of the protolith. In a Zr vs Nb diagram (Fig. 10a), the alignment of most of the samples clearly defines a magmatic trend suggesting that Nb can also be considered as an immobile element during weathering processes. This is consistent with the observations of relic pyrochlore-group minerals (a major host for Nb) together with zircon in several pedolith samples (Fig. 7c). Samples plotting outside the Zr-Nb magmatic differentiation trend are likely to derive mainly from a sedimentary protolith (mudstone – sites BH3 and BH4), but some magmatic contribution is required to explain the higher Zr and Nb contents of some samples. The latter is consistent with the observation of granitic dykelets cross-cutting the mudstone bedrock (Fig. 2). Very high Zr (> 5000 mg/kg) and Nb (> 1000 mg/kg) concentrations characterize regolith derived from granitic pegmatite dykes (sites BH1), whereas both elements are invariably low (< 400 mg/kg and < 150 mg/kg, respectively) in regolith formed from a syenitic protolith (sites BH2 and P3). In BH1, BH4, RS1, RS2 and P4, felsic dykes and trachyte were directly identified in the saprolite and in the saprock. Regolith samples from these sites have intermediate Nb (100–500 mg/kg) and Zr (1000–3000 mg/kg) contents overlapping with bulk data from peralkaline granitic dyke and trachyte from Estrade et al. (2014a). We thus consider that these samples mainly derive from felsic dykes and trachyte protoliths. In the central depression (sites P1 and P2), we have some evidence (surrounding boulders (Fig. 7J–L), high Al_2O_3 and Mn and low Ti contents (Fig. 10e and f)) indicating that the protolith is likely to be an SiO_2-undersaturated lithology. In this regolith, Zr and Nb contents are higher than in nepheline syenites mapped by Estrade et al. (2014a) suggesting that the lithology underlying the sites P1 and P2 is more evolved.

Total REE + Y content in regolith samples ranges from 150 to 5400 mg/kg with 85% of regolith samples below 2000 mg/kg (Fig. 10b). These grades are in the range of TREE + Y values reported

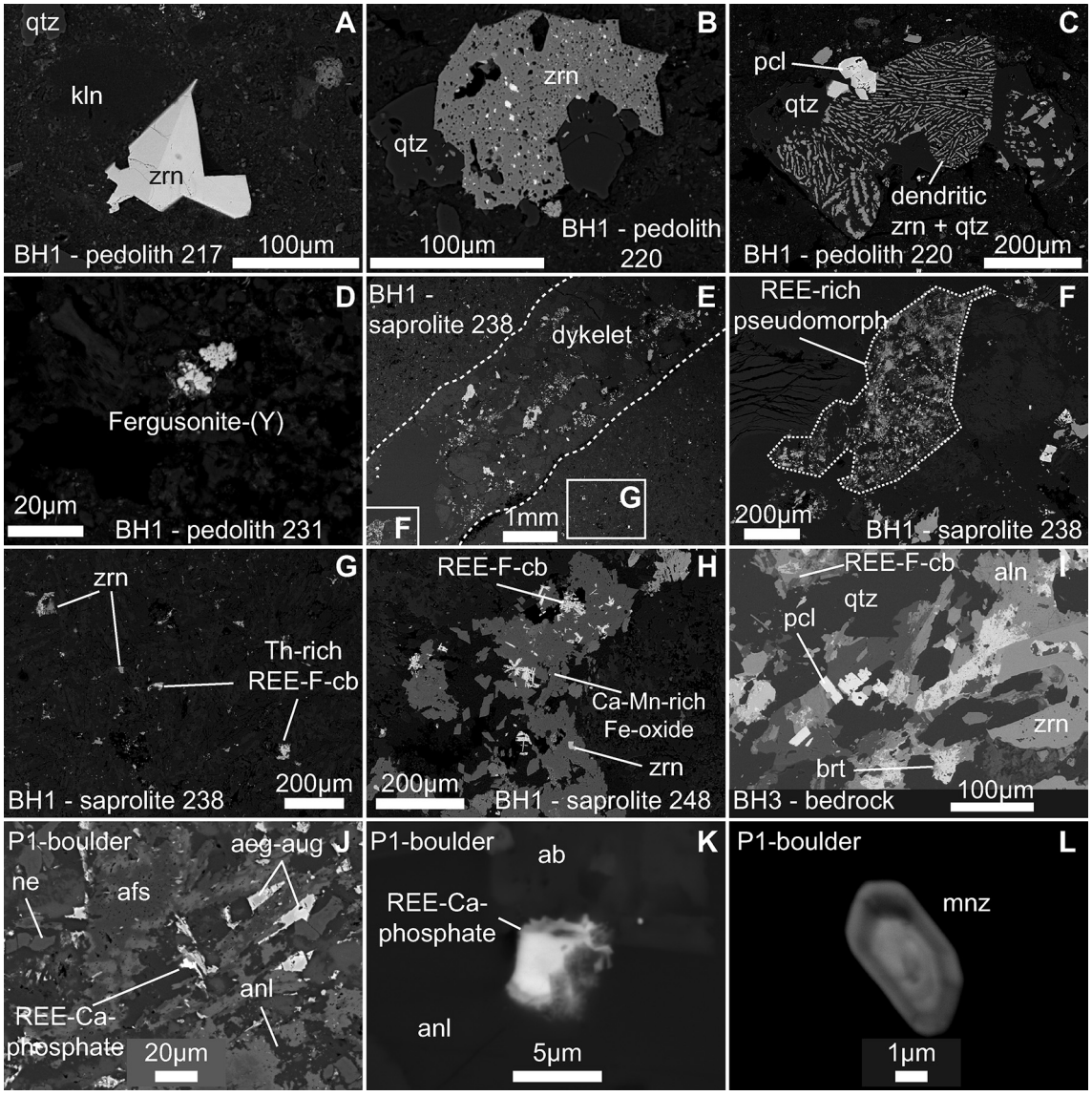

Fig. 7. BSE images of regolith samples from BH1 (A to H), bedrock sample from BH3 (I) and a boulder next to Pit 1 (J to L). For each image, the location of sample in the laterite profile and sample number are indicated. A – sector-zoned zircon (zrn) with quartz (qtz) and kaolinite (kln); B – porous and inclusion-rich zircon with quartz; C – Dendritic zircon with quartz and pyrochlore-group mineral (pcl); D – Fergusonite-(Y) grain; E – Granitic dykelet containing zircon and REE-rich phases in a trachyte; F – REE-rich pseudomorph located in the granitic dykelet from image E; G – Disseminated small grains of zircon and Th-rich REE-fluorcarbonates (REE-F-cb) in a trachyte; H – Ca-Mn-rich Fe oxide with REE-fluorcarbonates and zircon in the saprolite; I – Granitic dykelet containing allanite-Ce (aln), britholite-Ce (brt), quartz, pyrochlore-group mineral (pcl) and zircon; J to L – fine-grained nepheline-bearing syenite with aegirine-augite (aeg-aug), alkali feldspar (afs), analcime (anl), nepheline (ne), unidentified REE-Ca phosphate and monazite (mnz).

elsewhere for IADs (140 to 6500 mg/kg – see the compilation of Sanematsu and Watanabe (2016)). Among the 9 samples above 2000 mg/kg total REE, 6 samples derive from the pegmatite-rich protolith, 2 samples from the SiO_2-undersaturated rocks and 1 sample from a protolith of mudstone with granitic dykelets. Regolith formed from syenitic protolith has an invariably low total REE content (< 450 mg/kg). Among samples formed from the same protolith, LREE (excluding Ce) content varies up to 2 orders of magnitude, whereas HREE content variation is less than one order of magnitude (Fig. 10c and d). The positive correlation between Zr and HREE + Y observed for most of the samples suggests that HREE enrichment is mainly controlled by magmatic differentiation. In contrast, another process is required to explain the LREE enrichment, as it does not correlate with Zr. Among the major elements, absolute Al_2O_3 and Fe_2O_3 concentrations are increased by weathering but relative contents are mostly preserved during weathering processes, i.e. weathering of a protolith with high Al_2O_3 content forms regolith with high Al_2O_3 content and the same is true for Fe_2O_3 (Fig. 10e). Lastly, regolith presumably formed from SiO_2-undersaturated lithologies has a Ti content invariably below 1000 mg/kg and a relatively high Mn content (> 300 mg/kg) whereas all the other regoliths have a higher Ti content (Fig. 10f). This is consistent with the low Ti and high Mn contents of nepheline syenite cropping out in the area (Estrade et al., 2014a).

6.3. Leaching

6.3.1. Rare earth elements

We leached a total of 105 samples with ammonium sulfate and 30 samples with magnesium chloride, and analysed the leachates to quantify the contents of easily recoverable REE. Overall, all the chondrite-normalized REE patterns of the leachates have a similar shape to their corresponding bulk analyses of the laterite material. They all show

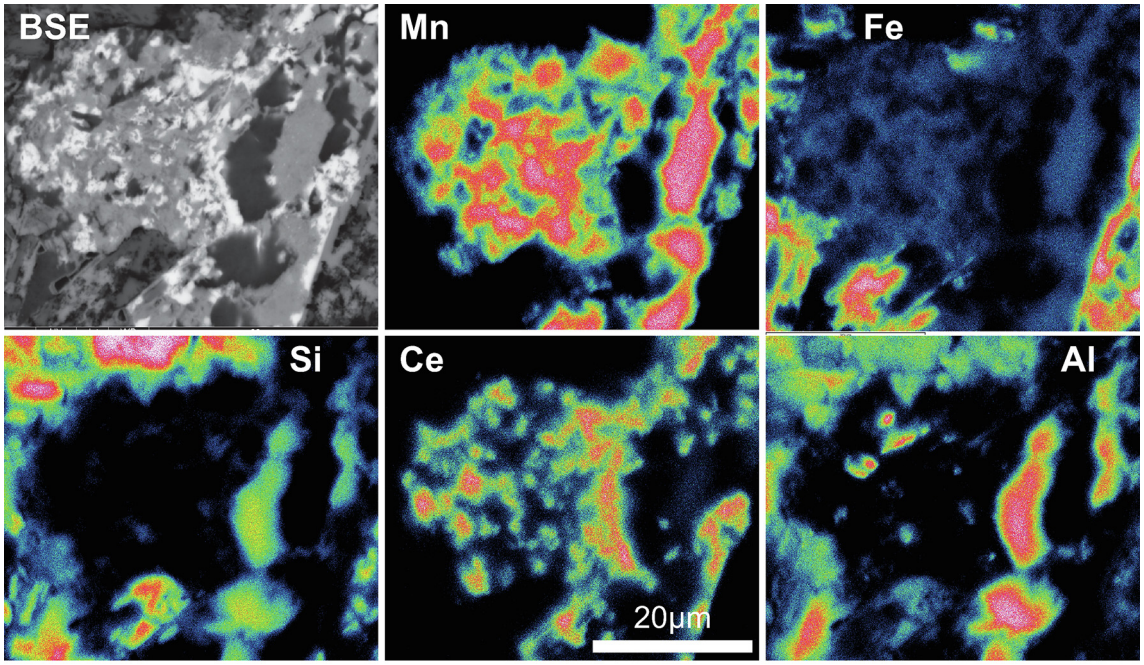

Fig. 8. BSE image and X-ray maps showing the distribution of manganese (Mn), iron (Fe), silicon (Si), cerium (Ce) and aluminium (Al) in saprolith sample 520 from Pit 2.

a negative Eu anomaly and are enriched in the LREE relative to the HREE, except for Ce which has a unique behaviour through laterite profiles (Fig. 11). In the upper pedolith (pedolith - soil), chondrite-normalized REE patterns of leachate either show a positive Ce anomaly or no anomaly ($Ce/Ce^* \geq 1$) which progressively evolves to a negative Ce anomaly in deeper horizons. This behaviour is not observed in the pit dug on the top of the syenite ridge (P3, Fig. 11i): throughout this profile, chondrite-normalized REE patterns display a constant positive Ce anomaly. All the leachate profiles are characterized by a negative LREE slope ($4 < La_N/Sm_N < 18$) whereas HREE slope varies depending on the nature of the bedrock. Leachates from laterite formed in the central depression have a flat HREE profile ($1 < Gd_N/Yb_N < 2$) (Fig. 11g and h and Fig. 12a) whereas other samples typically have a negative slope in their HREE profile ($3 < Gd_N/Yb_N < 10$). Leachate samples from saprock in BH1 have a significantly higher Gd_N/Yb_N ratio (20 and 30).

Overall, the amount of easily recoverable REE continuously increases with depth down to the saprolite and then decreases in the saprock. This trend is well observed in the pits except in P3, in which the content of easily recoverable REE starts to decrease above the transition between pedolith and saprolite (Fig. 11i). In the boreholes, this trend is disturbed by local increase or decrease of the concentration of leachable REE. For example in BH1 and BH3, in the middle of the pedolith, there is a strong increase in the concentration of leachable REE (from about 200 to 800 mg/kg TREE + Y, Fig. 11a and c) whereas in BH4 there is a strong decrease at the base of the pedolith. Such features are likely to be due to bedrock variation.

Among the 105 samples leached with ammonium sulfate, concentrations of easily recoverable REE range from 5 to 2300 mg/kg with 90% of the data ranging from 5 to 650 mg/kg (Fig. 12b). Samples leached with magnesium chloride generally released similar REE contents except in the lower saprolite (sample 238) and lower saprock (sample 246) in BH1 where much lower REE contents were leached. The LREE largely dominate (68–99%) over the HREE + Y (1–32% of which 40–68% Y). The LREE (excluding Ce)/ (TREE + Y) ratio, ranging from 0.08 to 0.92, tends to increase when TREE + Y increases (Fig. 12c). Overall, there is no clear correlation between horizon type and TREE + Y concentration although the 3 highest concentrations (> 1500 mg/kg) are in samples of saprolite and saprock (Fig. 12d). In some profiles, there are relatively high concentrations of leachable REE at transitions between horizons, for example at the base of the pedolith where it grades into saprolite. High concentrations (> 500 mg/kg) of easily recoverable REE are associated with varied bedrock lithologies (Fig. 12c).

The percentage of REE recovered in the ammonium sulfate leachate as compared to the bulk rock depends on the rare earth atomic number, the depth of the sample in the laterite profile and the nature of the protolith (Fig. 13). Overall, LREE (excluding Ce) are more easily leached than HREE + Y but this difference tends to decrease with depth. The LREE (excluding Ce) recovery rate is generally > 40% except in the lower pedolith in BH1 and in most of the P3 samples. The HREE recovery rate is highly variable along a same profile and in the different profiles.

6.3.2. *Major and trace elements*

Of the major elements analysed in the ammonium sulfate leachate, Al is the only cation measured at comparable concentrations to the LREE (1–10 mg/Kg, Fig. 14). Concentrations of other major elements Mg, Ca, K, and Mn are mostly below 1 mg/kg and Fe is always below detection limit. Only Al and Mn show a positive correlation with the concentration of leachable REE (albeit with protolith dependent trends), inferred to indicate the removal of the REE from clay minerals, and the association of Ce^{4+} with Mn oxides. There is no correlation with Ca or Mg, supporting the conclusion that the leachable REE are not associated with carbonates. Of the trace elements analysed only Se, Ba, U and Th were consistently above detection limits, and all were at lower concentration levels than the REE (µg/kg rather than mg/kg). Of these Se and Ba show positive correlation with leachable REE (albeit with protolith dependent trends) indicating similar mineralogical host and geochemical behaviour within the profiles, whilst U and Th show no significant correlation. The latter is significant as it indicates clear separation in behaviour between the lanthanides and actinides during weathering.

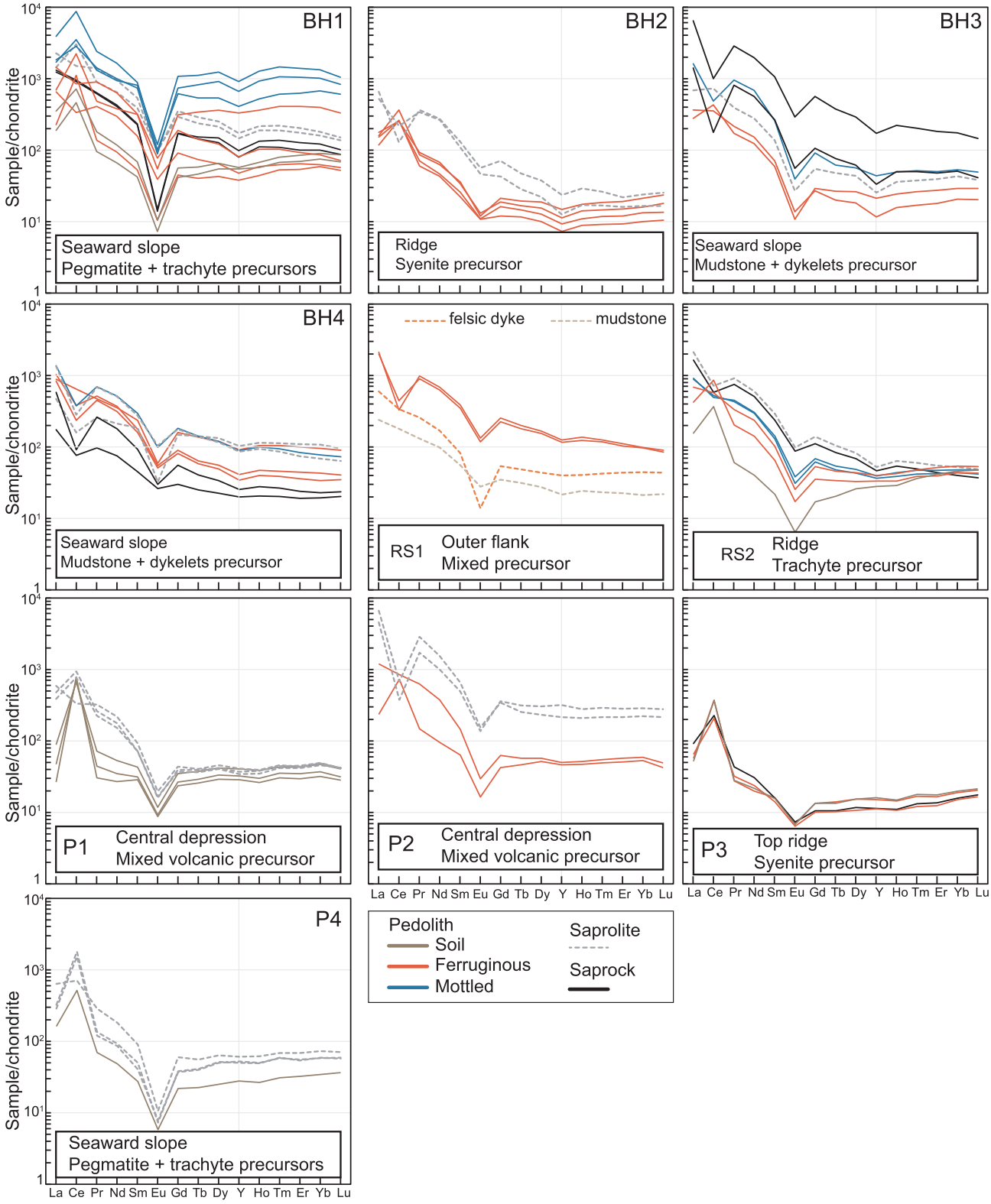

Fig. 9. Whole-rock REE distribution patterns normalized to CI chondrites values (McDonough and Sun, 1995) for each laterite profile.

7. Discussion

7.1. Controls on easily leachable REE distribution

7.1.1. Control from depth of weathering

Analyses of laterite profiles from across the Ambohimirahavavy complex show that the distribution of leachable REE is heterogeneous within any individual profile but is comparable between profiles (Fig. 11). Overall, laterite profiles typically show a leached upper part (pedolith-soil typically < 200 mg/kg TREE + Y) then an increasing concentration of easily leachable TREE + Y with depth. The highest concentrations are typically found into the saprolite (e.g. BH2, BH4, RS2, P1, P2 and P4) but significant leachable REE contents are also present locally into the pedolith (e.g. BH1 and BH3) and the saprock

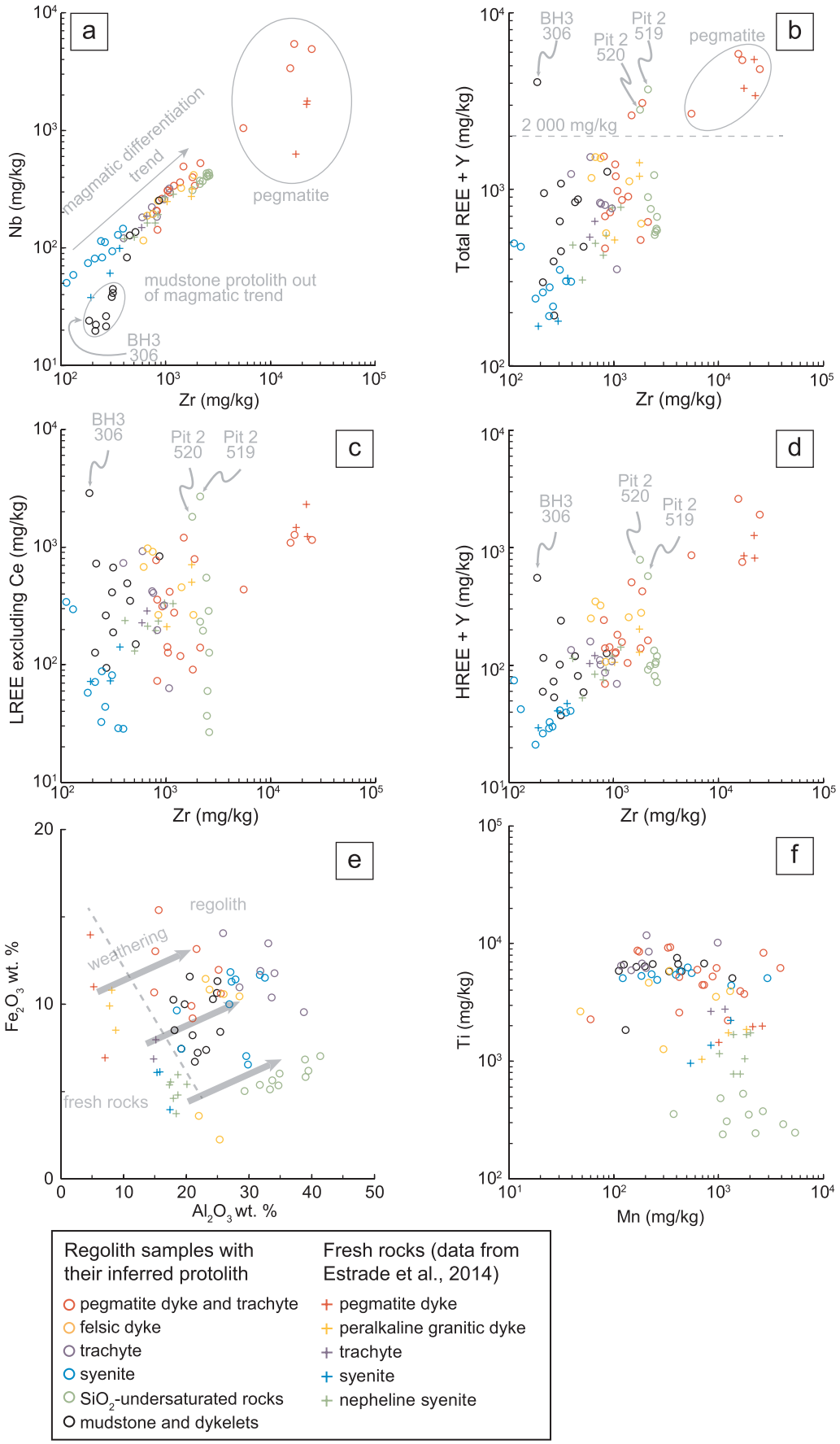

Fig. 10. Trace-element binary diagrams from regolith whole-rock data (circles) compared with fresh rocks whole-rock data (crosses) from Estrade et al. (2014a).

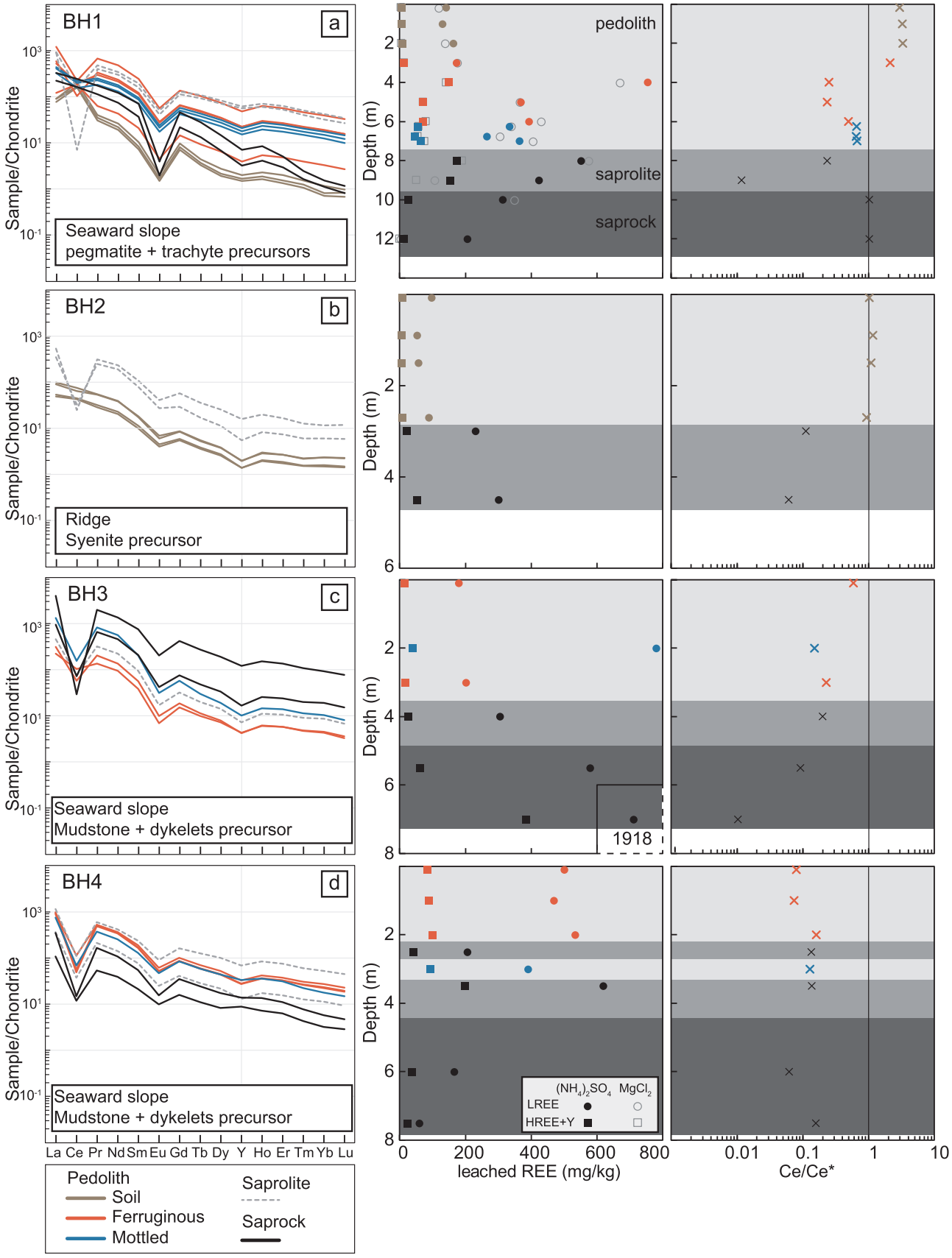

Fig. 11. For each laterite profile, chondrite normalized (using data from McDonough and Sun, 1995) REE distribution patterns, variation of leached REE concentration ($(NH_4)_2SO_4$ and $MgCl_2$) with depth and variation of Ce anomaly with depth. Ce anomaly calculated as $Ce/Ce^* = Ce_N/[(La_N*Pr_N)^{1/2}]$.

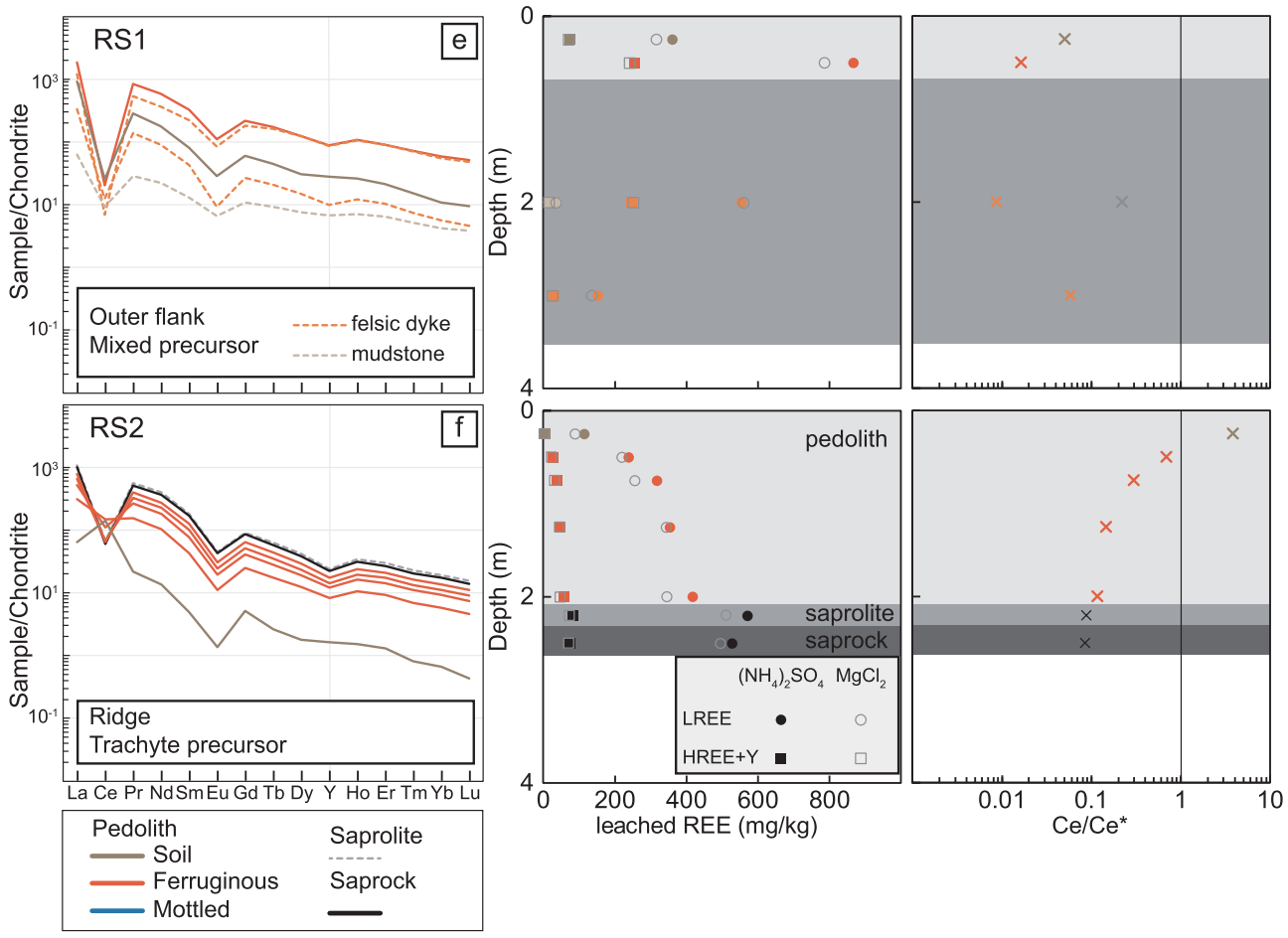

Fig. 11. (*continued*)

(e.g. BH3). The leached upper part missing in BH3 and BH4 was probably removed during the building of pad for the drillhole.

Easily leachable REE in IADs are usually attributed to adsorption onto clays but the precise nature and exact proportion of clays are rarely assessed. In the Ambohimirahavavy complex, kaolinite and halloysites (7 Å and 10 Å) are the main clays detected in all laterite profiles with relative halloysite proportion increasing with depth (Fig. 5 and Appendix). Halloysite proportion is usually higher in the lower pedolith and in the saprolite compared to the upper pedolith (Fig. 3). These laterite levels also contain a higher proportion of easily leachable REE (Fig. 11). Although the REE adsorption capacity of halloysites is not well known compared to kaolinite, they could play a significant role in the formation of IADs. Indeed, the range of cation exchange capacity determined for halloysite (2–60 cmol (+) kg^{-1}) is higher than kaolinite (1–15 cmol (+) kg^{-1}) (Joussein et al., 2005). Moreover, because many halloysites adopt unusual tubular morphology, they have a higher specific surface area than kaolinite, potentially increasing their exchange capacity (Hillier et al., 2016; Joussein et al., 2005). We could thus infer that in saprolite, the higher easily leachable REE content could be related to higher halloysite content. However, the apparent higher proportion of halloysite with depth could be due to the difficulty in differentiating between 7 Å-halloysite and kaolinite with XRD data in the upper part of laterite profiles. Indeed, as 10 Å-halloysite is easily and irreversibly transformed into 7 Å-halloysite by dehydration, it is likely that in the upper part of laterite profiles, which is subject to seasonal fluctuations of water table depth, 10 Å-halloysite was systematically dehydrated to 7 Å-halloysite.

The concentration of leachable REE at lithological/pedological contacts within laterite profiles is inferred to relate to significant hydraulic conductivity (K) contrasts resulting in the retention of water at levels corresponding to sharp drops in K. Despite a general lack of data on the hydraulic properties of laterite, extreme permeability variations with significant decreases in depth have been noted in previous studies (Bonsor et al., 2013). The preferential flow of infiltrating groundwater along such contacts resulted in a higher elemental flux over time and an extended period of groundwater residence. The increased element flux, coupled with an extended time period for sorption and a shift in geochemical conditions towards high pH conducive to lanthanide sorption on kaolinite (Coppin et al., 2002) as a result of water–rock interaction, all potentially contributed to REE concentration at this level. Increase in REE concentration where a contrast in hydraulic conductivity would be expected has been noted in a number of previous studies. These contrasts occur at the base of laterite profiles (Fernández-Caliani, 2018; Sanematsu et al., 2011; Viers and Wasserburg, 2004), at the pedolith/saprolite contact (Berger et al., 2014; Janots et al., 2015) or at levels of water table fluctuation (Braun et al., 2018).

7.1.2. Control from topography and hydrogeology

The topographic profile across the Ambohimirahavavy complex is characterized by steep hills and a relatively flat area in the central depression providing an ideal case to study the topographic effect on REE distribution in regolith (Fig. 2). At the top of the ridge (site P3), the bulk REE patterns of the regolith show a constant positive Ce anomaly throughout the profile and overall REE contents up to an order of magnitude lower than other pedolith and saprolite samples (Fig. 9). Other profiles usually have a positive Ce anomaly in their upper part which is either decreasing in amplitude or inverted to a negative anomaly downward, with a corresponding increase of REE content. These latter distributions in Ce anomaly have been noted in other studies. Sanematsu and Watanabe (2016) noted that the typical

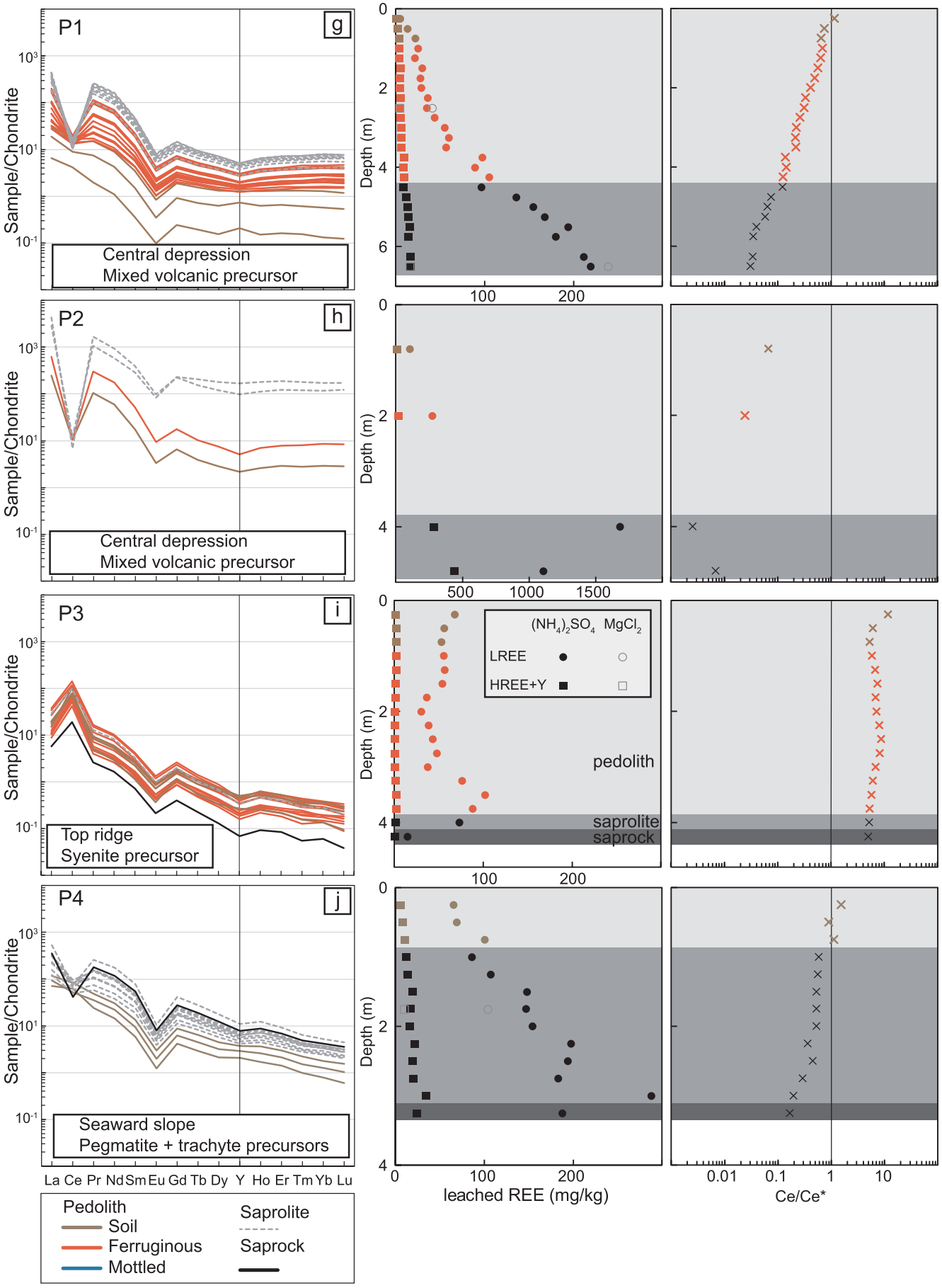

Fig. 11. (*continued*)

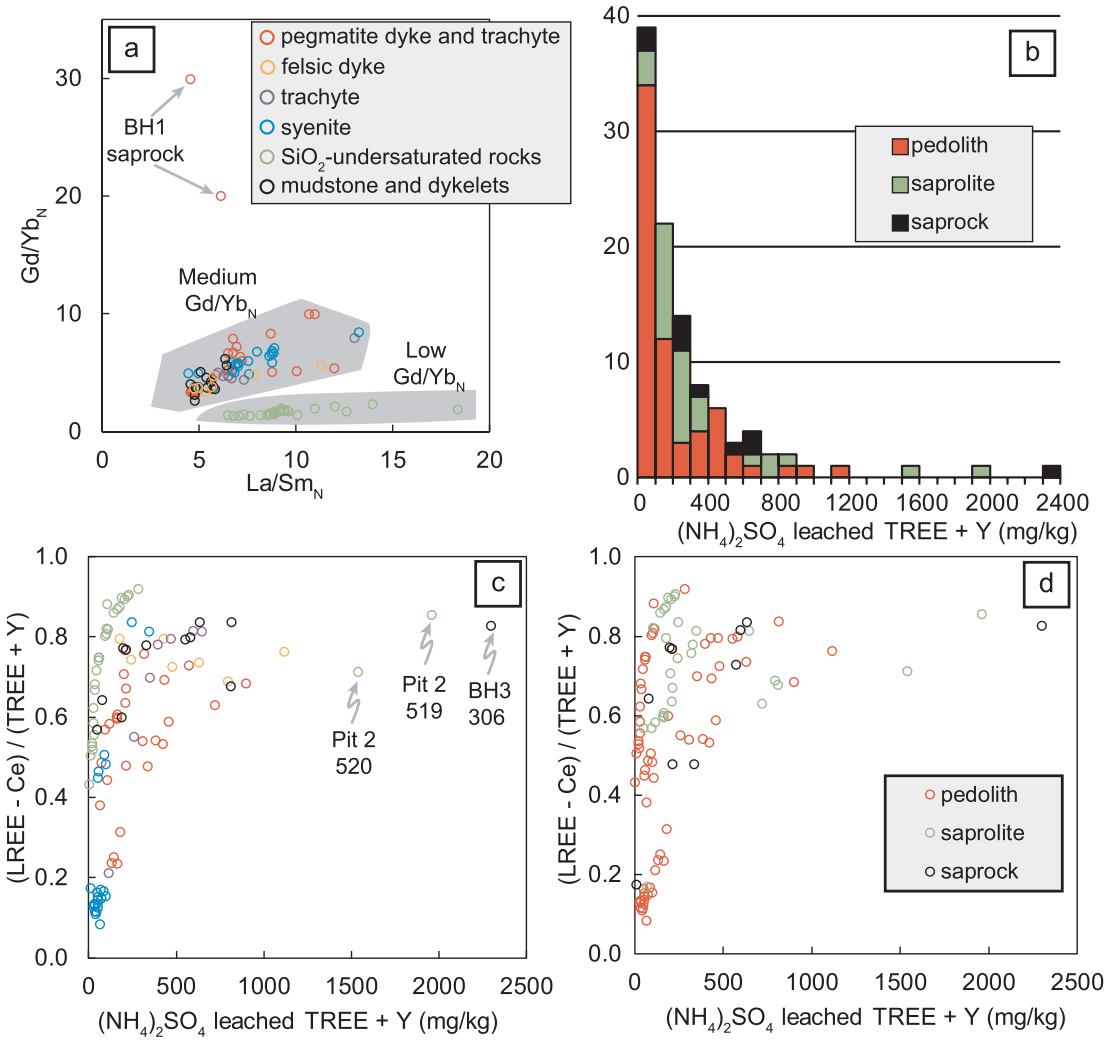

Fig. 12. (a-c-d) Binary diagrams of leached-REE data and (b) histogram of leached-REE concentration in regolith samples.

weathering profile of IADs from southern China has an upper REE-leached zone displaying a positive Ce anomaly and a lower REE-accumulation zone with a negative Ce anomaly. This anomaly results from the oxidation of Ce^{3+} to Ce^{4+} in the upper part of the profiles and the low solubility of Ce^{4+} relative to the other REE^{3+} in low temperature acidic soil solutions. Thus, because of its low mobility, Ce^{4+} is accumulated in the upper part of the profile, typically as cerianite or associated with Mn oxyhydroxides (Fig. 8), whereas other REE are leached and accumulated in the lower part of the profile. The constant positive anomaly at the top of the ridge also suggests that Ce has not been leached during weathering compared to the other REE. However, the similar recovery percentage of Ce and LREE leached with ammonium sulfate all along the profile indicates that a similar proportion of Ce and LREE are weakly adsorbed onto clays (Fig. 13). In all the other profiles, the much lower recovery percentage of Ce compared to the other LREE is consistent with Ce^{4+} mainly contained within cerianite as this mineral is not dissolved by ammonium sulfate.

Recently, Berger et al. (2014) and Janots et al. (2015) studied a single weathering profile in central Madagascar. They noted a strong positive Ce anomaly in the B horizon (pedolith-ferruginous and pedolith-mottled zones in this study), associated with highest TREE content. Janots et al. (2015) conducted a XANES study and identified Ce^{4+} contained within cerianite associated with Mn oxyhydroxides. $Cerium^{3+}$ was dominantly hosted in secondary phosphates and adsorbed onto clays. Similar patterns are observed in bulk rock data from this study (Fig. 9), but there is a contrast in the leachable fraction and in the spatial distribution of positive Ce anomalies (Fig. 11). Within the bulk rock data positive Ce anomalies occur in soil, ferruginous and mottled zones, but with the leaching data positive Ce anomalies are only developed in the soil zone, or in the ferruginous zone at topographic highs. This is consistent with Ce oxidation during weathering producing leachable Ce^{4+} in the soil zone which is subsequently fixed as insoluble cerianite associated with Mn oxyhydroxides. The strong localisation of positive Ce anomalies at topographic highs was not noted by Berger et al. (2014) and Janots et al. (2015), but they only addressed a single vertical profile. Immobilisation of Ce^{3+} as secondary phosphates is also limited at Ambohimirahavavy as phosphate contents are low in the bedrock.

The use of multiple profiles in our study means that the effects of topography can be evaluated in more detail. The lack of a simple bedrock source precludes full mass balance analysis, but the data are consistent with REE leaching at topographic highs, with the REE-enriched groundwater generated flowing downslope. The thick unsaturated zone at higher elevation meant that oxidising conditions prevailed and Ce was preferentially retained by oxidisation to Ce^{4+}. The effects of topography on the spatial distribution of REE in laterite have been previously considered by Braun et al. (2018). They concluded that REE and Y loss was not significant in ridge-top saprolite. Significant REE losses were related to pedogenic processes, notably in ferralsol (saprolite in this study) and vertisol (laterite transported as colluvium).

It is notable in this study that no level in the profiles showed overall

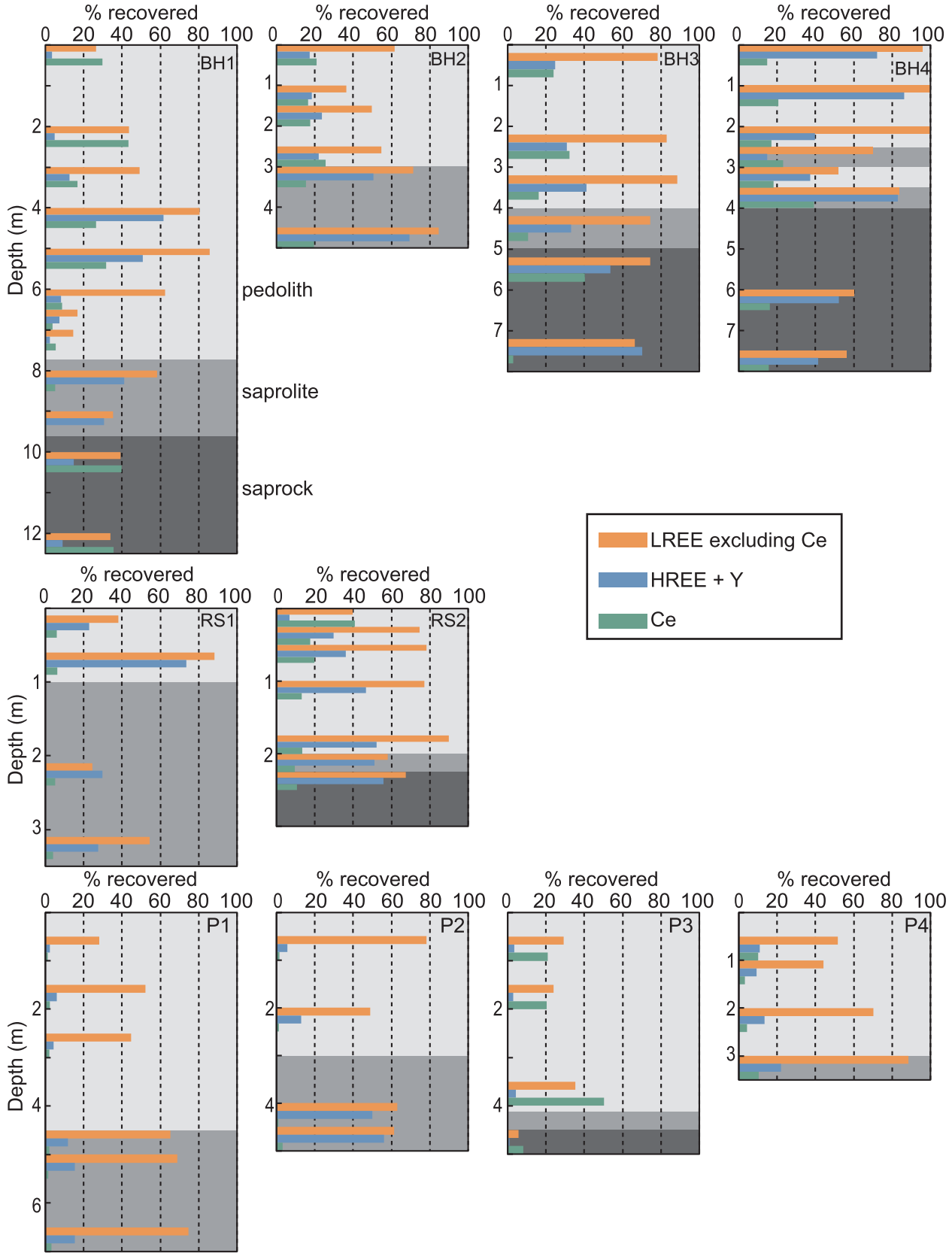

Fig. 13. Vertical profiles from the different laterite profiles showing histograms at different depth of the percentage of leached LREE excluding Ce (orange), HREE + Y (blue) and Ce (green). (For interpretation of the references to colour in this figure legend, the reader is referred to the web version of this article.)

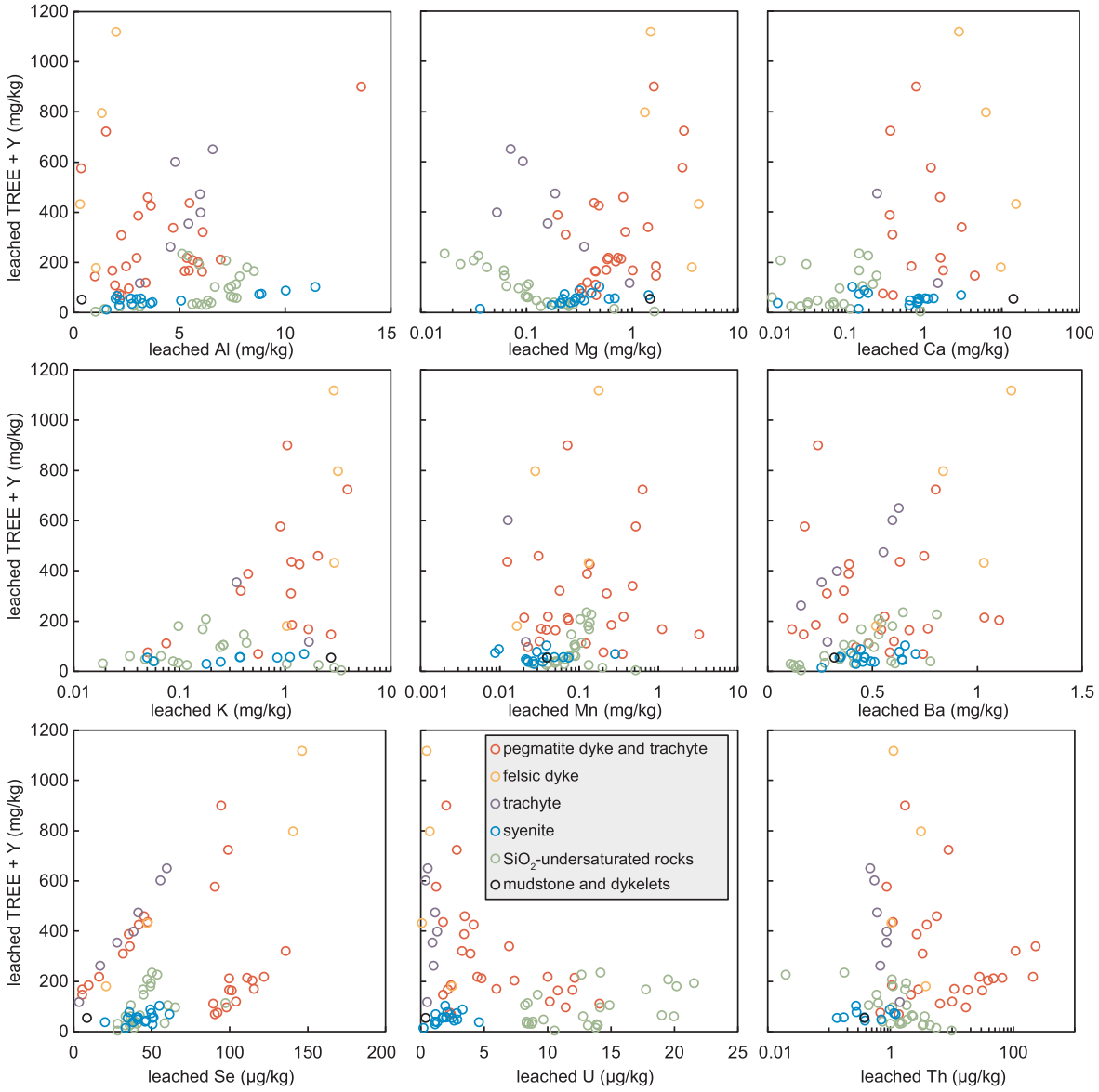

Fig. 14. Binary diagrams for various major and trace elements leached with $(NH_4)_2SO_4$.

enrichment in the REE relative to bedrock. The lack of comparable control on REE from topographically controlled hydrology can be attributed to differences in bedrock mineralogy. In Braun et al.'s study (2018) the REE distribution was controlled by the relative proportions of resistant (thorite, monazite, zircon) or more reactive (titanite, allanite, bastnäsite, apatite) REE or REE-bearing minerals and the re-mineralisation of the REE as secondary phosphates (rhabdophane) alongside carbonates and oxides. The REE were inferred to be removed from the profiles in solution in the soil zone, and transported as suspended particulates of insoluble phases throughout. The difference in behaviour, where this study showed clear evidence of REE leaching and Ce oxidation at topographic highs in contrast to the conclusion of Braun et al. (2018), is again related to the bedrock mineralogy, and in particular phosphate concentration, in the protolith.

7.1.3. Influence of parent rock

In IADs, the geochemical characteristics of the regolith are largely inherited from its parental rock and its mineralogical content. In currently mined IADs, the LREE or HREE-rich IADs are typically formed from LREE or HREE-rich granitoids respectively (Li et al., 2017). The nature of the main REE-bearing minerals in these granitoids is one of the key parameters for the formation of valuable IADs. A favourable bedrock would contain REE in easily decomposed minerals such as REE fluorcarbonates whereas less favourable bedrock might contain weathering resistant zircon, monazite and xenotime. In the Ambohimirahavavy complex, the regolith formed from a large variety of bedrock protoliths ranging from sedimentary (typically mudstone) to alkaline magmatic lithologies. These protoliths have highly variable bulk TREE + Y contents ranging from 200 to 5800 mg/kg, including > 55% of LREE (Fig. 10). Although the highest bulk REE concentrations are associated with regolith derived from granitic pegmatite dykes (Fig. 10b), these lithologies are not the most favourable for the formation of IAD as they only contain a small percentage of easily leachable REE (Fig. 15). For example, the two samples in BH1 with the highest bulk HREE + Y content (samples 230 and 231; > 1500 mg/kg) and high LREE (excluding Ce) content (> 1000 mg/kg) released < 10% and < 25% of their bulk HREE + Y and LREE respectively when leached with ammonium sulfate. This low leachable REE content is consistent with the weathering resistant nature of the two main REE hosts identified in these lithologies, zircon and pyrochlore-group minerals (Fig. 7A to C). Moreover, the very low LREE (excluding Ce) / HREE + Y (0.4 and 0.6) bulk ratios, compared to all the other samples, are

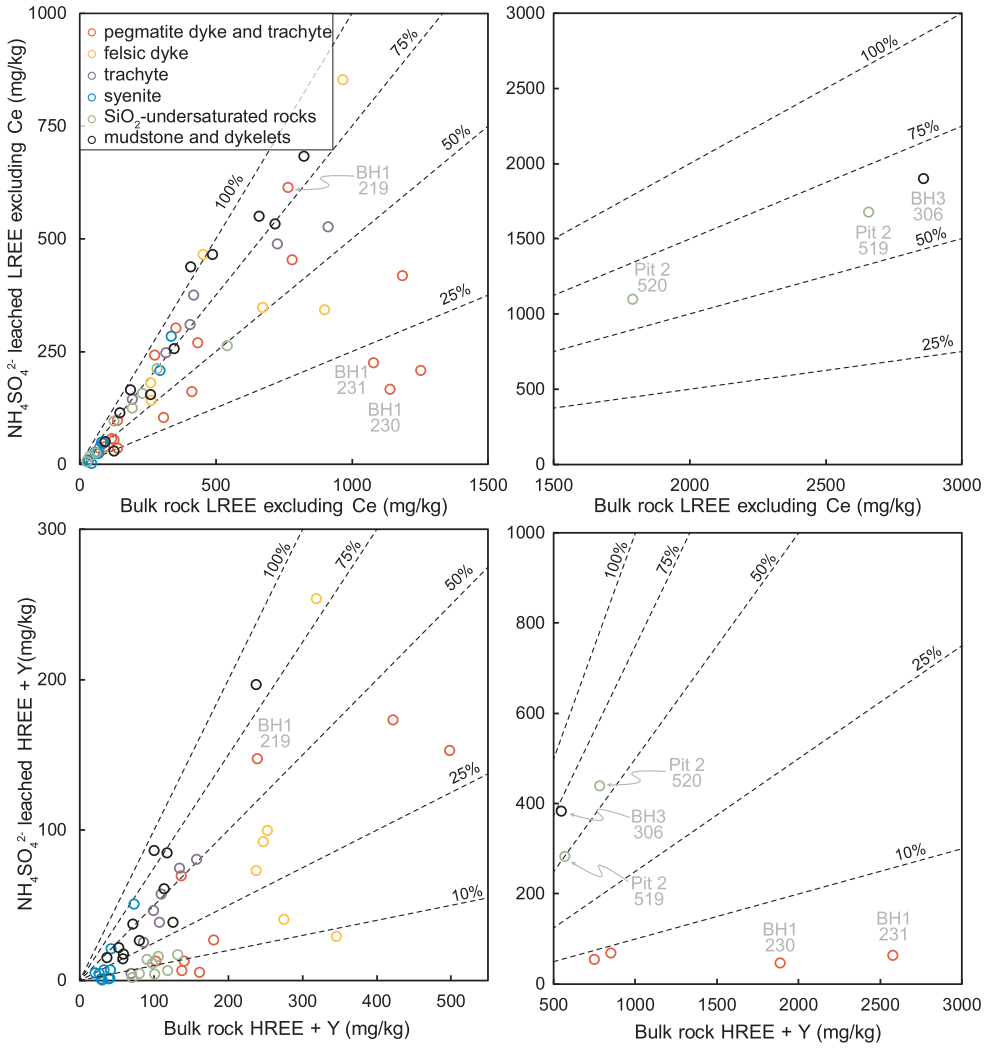

Fig. 15. Diagrams of $(NH_4)_2SO_4$ leached versus bulk rock LREE (excluding Ce) and HREE + Y (mg/kg) in regolith samples. Dashed lines show the percentage of extraction.

consistent with zircon as a major REE host in these samples (zircon is typically enriched in HREE, see Hoskin and Schaltegger (2003) and references therein). However, locally in the pedolith of BH1 (sample 219), > 50% of HREE + Y and > 75% of LREE (excluding Ce) were released, suggesting that other easily weatherable minerals could host REE. Estrade et al. (2014b) studied in detail the mineralogy of peralkaline granitic and pegmatitic dykes from the Ambohimirahavavy complex. They noted that REE-bearing minerals occur either as magmatic or hydrothermal phases and further subdivided magmatic phases into miaskitic and agpaitic assemblages. In this latter assemblage, the main agpaitic mineral identified is an eudialyte-group mineral, a REE-bearing zirconosilicate (Estrade et al., 2018). This mineral, as most agpaitic minerals in peralkaline granite, is very commonly altered by late-magmatic fluids and replaced by complex secondary assemblages where zircon is commonly present (Borst et al., 2016; Estrade et al., 2018). Therefore, we inferred that this mineral is very prone to weathering, making the agpaitic granite a good candidate to release a significant amount of REE. Alternatively, replacive hydrothermal assemblages can also be a good precursor provided that zircon is not the main replacing phase.

In terms of easily leachable REE content, the most favourable protoliths are the SiO_2-undersaturated lithology from the central depression (P1 and P2) and, unexpectedly, the mudstone with granitic dykelets from the seaward slope (BH3 and BH4). For example, samples with the highest bulk LREE (excluding Ce) concentrations (> 1500 mg/kg; 519 and 520 in P2 and 306 in BH3) have > 50% of easily leachable REE (Fig. 15). In samples derived from the mudstone with granitic dykelets, the low Zr content (< 1000 mg/kg) and the lack of correlation between Zr and TREE + Y (Fig. 10b) indicate that zircon is not the main REE-bearing mineral. This is consistent with our observations of allanite-(Ce) and REE-fluorcarbonates as the main REE-bearing minerals in these granitic dykelets, although a great variety of other REE-bearing minerals may also be present. In samples derived from the SiO_2-undersaturated protolith (sites P1 and P2), Zr content is relatively high (2000–3000 mg/kg) but one order of magnitude below zircon-rich samples derived from the pegmatitic granitic dykes (although they have similar TREE + Y content) indicating again that zircon is not the main REE-phase. The only REE-phases identified from a surrounding boulder are a REE-Ca phosphate and monazite (Fig. 7j-k-l) but this latter mineral is resistant to weathering. A noteworthy feature is that Estrade et al. (2014a) locally observed eudialyte grains in nepheline syenite next to P1 and P2 suggesting that an easily weatherable agpaitic phase could be also present in the bedrock. It is evident that more data from the bedrock are needed to explain the high proportion of easily leachable REE.

7.2. Overview of favourable conditions for the formation of IAD in the Ambohimirahavavy complex

Based on the detailed study of boreholes, pits and road sections, we

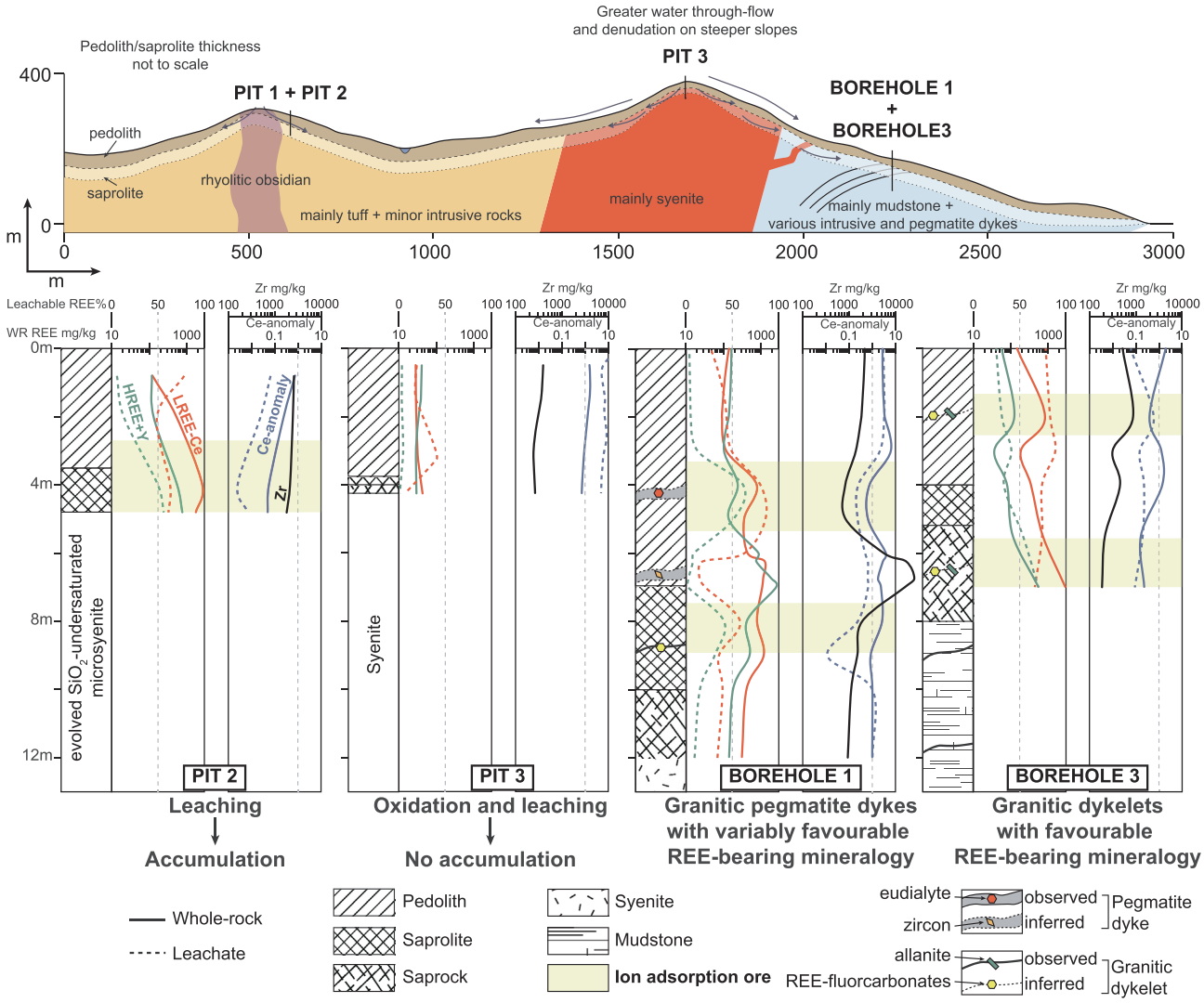

Fig. 16. Overview of favourable conditions for the formation of IAD in the Ambohimirahavavy complex. See the text for further explanations.

propose the following overview of favourable conditions for the formation of IAD in the Ambohimirahavavy alkaline complex (Fig. 16). At first order, the main control on the amount of leachable REE and the LREE/HREE proportion is the nature of the bedrock and most importantly the nature of primary REE-bearing minerals. The most favourable lithologies are the most evolved as they result from extended magmatic differentiation which has concentrated the REE. These highly differentiated lithologies can be either foid-bearing (nepheline syenite) or quartz-bearing (granitic pegmatite dykes and dykelets). Among these rocks, two types of mineralogy were favourable for the formation of IAD: (1) agpaitic mineralogy, including eudialyte-group mineral which occurs locally in granitic pegmatite dykes and SiO_2-undersaturated syenite and (2) allanite-(Ce) and REE-fluorcarbonates occurring mostly in granitic dykelets. These minerals were easily weathered by acidic percolating water and released their REE into the environment during laterite formation. However, in most of the granitic pegmatite dykes, primary agpaitic mineralogy was replaced during a late-magmatic hydrothermal event by secondary assemblages with weathering resistant zircon as a main HREE-bearing phase together with LREE-bearing fluorcarbonates. As a result, during laterite formation, these hydrothermally altered pegmatites keep a significant proportion of their REE (mainly HREE) locked up in zircon. At second order, topography and hydrography can locally control the amount of REE. At topographic highs, oxidising conditions prevailing in the unsaturated zone were not favourable for the adsorption of REE onto clays. Percolating water leached the REE from primary weathered minerals and flowed downslope.

8. Conclusions

Analysis of laterite profiles formed by weathering of the Ambohimirahavavy alkaline complex show that the REE distribution is heterogeneous, with control from both bedrock heterogeneity, and the hydrological variation between pedolith and saprolite.

- The clay fraction in all sites is dominated by kaolinite and halloysite (7 Å and 10 Å) with higher halloysite proportion in the lower pedolith and in the saprolite. Laterite levels with significant halloysite proportion also contain a higher proportion of easily leachable REE.
- Laterite profiles typically show a leached upper part then an increasing concentration of easily leachable TREE + Y with depth.
- The main control on leachable REE is not the amount of REE that is present in the bedrock, but the nature of the bedrock and the primary minerals that host the REE. The exact distribution of the REE within the laterite profiles is controlled by hydrological and topographic factors.
- IAD with the highest concentrations of easily leachable REE are likely to be found above bedrock protoliths that contain the REE in

weatherable minerals such as REE-fluorcarbonates, allanite-(Ce) or eudialyte-group mineral.
- LREE/HREE ratio in the regolith is inherited from the LREE/HREE ratio in the bedrock.
- Although autometasomatism is usually considered as a favourable process by the formation of minerals more susceptible to weathering, in peralkaline rocks, this process inhibited the formation of IAD by transforming easily weathered agpaitic mineralogy into unweatherable zircon.

Acknowledgements

We would like to thank Michael Haschke for providing samples. Rocky Lowell Rakotoson and Fetra Rasolonirina are thanked for their invaluable assistance in organising fieldwork in Madagascar. This paper is a product of the SoS RARE project which is funded by the UK's Natural Environment Research Council under Grant Agreement No. NE/M011429/1. KG publishes with the permission of the Executive Director, British Geological Survey

Appendix A. Supplementary data

Supplementary data to this article can be found online at https://doi.org/10.1016/j.oregeorev.2019.103027.

References

Bao, Z., Zhao, Z., 2008. Geochemistry of mineralization with exchangeable REY in the weathering crusts of granitic rocks in South China. Ore Geol. Rev. 33, 519–535. https://doi.org/10.1016/j.oregeorev.2007.03.005.

Berger, A., Janots, E., Gnos, E., Frei, R., Bernier, F., 2014. Rare earth element mineralogy and geochemistry in a laterite profile from Madagascar. Appl. Geochem. 41, 218–228. https://doi.org/10.1016/j.apgeochem.2013.12.013.

BGS-USGS-GLW, 2008. République de Madagascar Ministère de L'énergie et des Mines (MEM/SG/DG/UCP/PGRM). (British Geological Survey Research Report No. 78).

Bonsor, H.C., MacDonald, A.M., Davies, J., 2013. Evidence for extreme variations in the permeability of laterite from a detailed analysis of well behaviour in Nigeria. Hydrol. Process. 28, 3563–3573. https://doi.org/10.1002/hyp.9871.

Borst, A.M., Friis, H., Andersen, T., Nielsen, T.F.D., Waight, T.E., Smit, M.A., 2016. Zirconosilicates in the kakortokites of the Ilímaussaq complex, South Greenland: Implications for fluid evolution and high-field-strength and rare-earth element mineralization in agpaitic systems. Mineral. Mag. 80, 5–30.

Brantley, S.L., 2008. Kinetics of Mineral Dissolution. In: Brantley, S.L., Kubicki, J.D., White, A.F. (Eds.), Kinetics of Water-Rock Interaction. Springer New York, New York, NY, pp. 151–210 doi: 10.1007/978-0-387-73563-4_5.

Braun, J.-J., Riotte, J., Battacharya, S., Violette, A., Oliva, P., Prunier, J., Maréchal, J.-C., Ruiz, L., Audry, S., Subramanian, S., 2018. REY-Th-U Dynamics in the Critical Zone: Combined Influence of Reactive Bedrock Accessory Minerals, Authigenic Phases, and Hydrological Sorting (Mule Hole Watershed, South India). Geochem. Geophys. Geosystems 19, 1611–1635. https://doi.org/10.1029/2018GC007453.

Chakhmouradian, A.R., Wall, F., 2012. Rare earth elements: minerals, mines, magnets (and more). Elements 8, 333–340.

Coppin, F., Berger, G., Bauer, A., Castet, S., Loubet, M., 2002. Sorption of lanthanides on smectite and kaolinite. Chem. Geol. 182, 57–68.

Cucciniello, C., Tucker, R.D., Jourdan, F., Melluso, L., Morra, V., 2016. The age and petrogenesis of alkaline magmatism in the Ampasindava Peninsula and Nosy Be archipelago, northern Madagascar. Miner. Petrol. 110, 309–331. https://doi.org/10.1007/s00710-015-0387-1.

Davies, J., 2009. Hydrogeological mapping of north-central Madagascar using limited data. Presented at the Groundwater 2009 conference Cape Town, Cape Town, South Africa.

Desharnais, G., Camus, Y., Bisaillon, C., 2014. NI 43-101 Technical Report – resources for the Tantalus rare earth ionic clay project Northern Madagascar. SGS.

Eggleton, R.A., 2001. The regolith glossary: surficial geology, soils and landscapes, Cooperative Research Centre for Landscape Evolution and Mineral Exploration. ed.

Estrade, G., Béziat, D., Salvi, S., Tiepolo, M., Paquette, J.-L., Rakotovao, S., 2014a. Unusual evolution of silica-under- and -oversaturated alkaline rocks in the Cenozoic Ambohimirahavavy Complex (Madagascar): mineralogical and geochemical evidence. Lithos 206–207, 361–383. https://doi.org/10.1016/j.lithos.2014.08.008.

Estrade, G., Salvi, S., Béziat, D., 2018. Crystallisation and destabilisation of eudialyte-group minerals in peralkaline granite and pegmatite: a case study from the Ambohimirahavavy complex. Madagascar. Mineral. Mag. 1–59. https://doi.org/10.1180/minmag.2017.081.053.

Estrade, G., Salvi, S., Béziat, D., Rakotovao, S., Rakotondrazafy, R., 2014b. REE and HFSE mineralization in peralkaline granites of the Ambohimirahavavy alkaline complex, Ampasindava peninsula, Madagascar. J. Afr. Earth Sci. 94, 141–155. https://doi.org/10.1016/j.jafrearsci.2013.06.008.

Fernández-Caliani, J.C., 2018. Rare-earth element and stable isotope signatures of kaolin from a Pliocene lateritic weathering profile at mid-latitude region (Andalusia, Spain): implications for paleoweathering and paleoclimatic reconstructions. CATENA 167, 160–170. https://doi.org/10.1016/j.catena.2018.04.025.

Ganzeev, A.A., Grechishchev, O.K., 2003. A new genetic type of rare-metal alkali granites of Madagascar. Russ. Geol. Geophys. 44, 539–553.

Geiger, M., Schweigert, G., 2006. Toarcian-Kimmeridgian depositional cycles of the south-western Morondava Basin along the rifted continental margin of Madagascar. Facies 52, 85. https://doi.org/10.1007/s10347-005-0039-8.

Goodenough, K.M., Wall, F., Merriman, D., 2017. The rare earth elements: demand, global resources, and challenges for resourcing future generations. Nat. Resour. Res. https://doi.org/10.1007/s11053-017-9336-5.

Hillier, S., Brydson, R., Delbos, E., Fraser, T., Gray, N., Pendlowski, H., Phillips, I., Robertson, J., Wilson, I., 2016. Correlations among the mineralogical and physical properties of halloysite nanotubes (HNTs). Clay Miner. 51, 325–350. https://doi.org/10.1180/claymin.2016.051.3.11.

Hodson, M.E., 2002. Experimental evidence for mobility of Zr and other trace elements in soils. Geochim. Cosmochim. Acta 66, 819–828. https://doi.org/10.1016/S0016-7037(01)00803-1.

Hoskin, P.W.O., Schaltegger, U., 2003. The composition of zircon and igneous and metamorphic petrogenesis. Rev. Mineral. Geochem. 53, 27–62. https://doi.org/10.2113/0530027.

Janots, E., Bernier, F., Brunet, F., Muñoz, M., Trcera, N., Berger, A., Lanson, M., 2015. Ce (III) and Ce(IV) (re)distribution and fractionation in a laterite profile from Madagascar: Insights from in situ XANES spectroscopy at the Ce LIII-edge. Geochim. Cosmochim. Acta 153, 134–148. https://doi.org/10.1016/j.gca.2015.01.009.

Joussein, E., Petit, S., Churchman, J., Theng, B., Righi, D., Delvaux, B., 2005. Halloysite clay minerals — a review. Clay Miner. 40, 383–426. https://doi.org/10.1180/0009855054040180.

Li, Y.H.M., Zhao, W.W., Zhou, M.-F., 2017. Nature of parent rocks, mineralization styles and ore genesis of regolith-hosted REE deposits in South China: an integrated genetic model. J. Asian Earth Sci. 148, 65–95. https://doi.org/10.1016/j.jseaes.2017.08.004.

Madejová, J., 2003. FTIR techniques in clay mineral studies. Vib. Spectrosc. 31, 1–10. https://doi.org/10.1016/S0924-2031(02)00065-6.

McDonough, W.F., Sun, S.S., 1995. The composition of the earth. Chem. Geol. 120, 223–253. https://doi.org/10.1016/0009-2541(94)00140-4.

Melluso, L., Morra, V., Brotzu, P., Franciosi, L., Grifa, C., Lustrino, M., Morbidelli, P., Riziky, H., Vincent, M., 2007. The Cenozoic alkaline magmatism in central-northern Madagascar: a brief overview. Period. Mineral. 76, 169–180. https://doi.org/10.2451/2007pm0023.

Moldoveanu, G.A., Papangelakis, V.G., 2016. An overview of rare-earth recovery by ion-exchange leaching from ion-adsorption clays of various origins. Mineral. Mag. 80, 63–76. https://doi.org/10.1180/minmag.2016.080.051.

Packey, D.J., Kingsnorth, D., 2016. The impact of unregulated ionic clay rare earth mining in China. Resour. Policy 48, 112–116. https://doi.org/10.1016/j.resourpol.2016.03.003.

Rauret, G., Lopez-Sanchez, J.F., Lück, D., Yli-Halla, M., Muntau, H., Quevauviller, P., 2001. EUR-19775 – The certification of the extractable contents (mass fractions) of Cd, Cr, Cu, Ni, Pb and Zn in freshwater sediment following sequential extraction procedure BCR-701, BCR information series. European Commission.

Russell, J.D., Fraser, A.R., 1994. Infrared methods. In: Wilson, M.J. (Ed.), Clay Mineralogy: Spectroscopic and Chemical Determinative Methods. Chapman & Hall, pp. 367.

Sanematsu, K., Kon, Y., 2013. Geochemical characteristics determined by multiple extraction from ion-adsorption type REE ores in Dingnan County of Jiangxi Province. South China 64, 313–330.

Sanematsu, K., Moriyama, T., Sotouky, L., Watanabe, Y., 2011. Mobility of rare earth elements in basalt-derived laterite at the bolaven plateau, Southern laos. Resour. Geol. 61, 140–158. https://doi.org/10.1111/j.1751-3928.2011.00155.x.

Sanematsu, K., Watanabe, Y., 2016. Characteristics and genesis of ion adsorption-type rare earth element deposits. In: Verplanck, P.L., Hitzman, M.W. (Eds.), Rare Earth and Critical Elements in Ore Deposits. Society of Economic Geologists p. 0. https://doi.org/10.5382/Rev.18.03.

Viers, J., Wasserburg, G.J., 2004. Behavior of Sm and Nd in a lateritic soil profile. Geochim. Cosmochim. Acta 68, 2043–2054. https://doi.org/10.1016/j.gca.2003.10.034.

Wall, F., Rollat, A., Pell, R.S., 2017. Responsible sourcing of critical metals. Elements 13, 313–318. https://doi.org/10.2138/gselements.13.5.313.

Xu, C., Kynický, J., Smith, M.P., Kopriva, A., Brtnický, M., Urubek, T., Yang, Y., Zhao, Z., He, C., Song, W., 2017. Origin of heavy rare earth mineralization in South China 8, 14598.

Yang, X.J., Lin, A., Li, X.-L., Wu, Y., Zhou, W., Chen, Z., 2013. China's ion-adsorption rare earth resources, mining consequences and preservation. Environ. Dev. 8, 131–136. https://doi.org/10.1016/j.envdev.2013.03.006.